Detection of dilution due to turbulent mixing ~~and~~vs. precipitation scavenging effects on biomass burning ~~aerosols~~aerosol concentrations using ~~total~~stable water ~~heavy~~ isotope ratios during ORACLES

Dean Henze[1], David Noone[1,2], Darin Toohey[3]

[1] College of Earth, Ocean, and Atmospheric Sciences, Oregon State University, Corvallis, OR, U.S.A.
[2] Department of Physics, Waipapa Taumata Rau-The University of Auckland, Auckland, New Zealand
[3] Department of Atmospheric and Oceanic Sciences, University of Colorado Boulder, Boulder, CO, U.S.A.

Correspondence to: Dean Henze (henzede@oregonstate.edu), David Noone (david.noone@auckland.ac.nz)

Abstract. The interaction between biomass burning aerosols and clouds remains challenging to accurately determine, in part because of difficulties ~~in~~ using direct observations to account for influences ~~of~~on aerosol concentrations from precipitation scavenging and dilution ~~separately from sources~~due to air mass mixing and separating those signals from source contributions. The prevalence of mixing versus precipitation processes in biomass burning aerosol (BBA) laden air ~~over~~ in the southeast Atlantic lower free troposphere (FT) and marine boundary layer (MBL) is assessed during three ~~intensive~~ observation periods (September 2016, August 2017, and October 2018) during the NASA ORACLES (ObseRvations of Aerosols above CLouds and their intEractionS) campaign. ~~**Air in the lower free troposphere (FT) and marine boundary layer (MBL) are distinct, and can be treated as separate**~~Significant sources of BBA's over the African continent combined with regional circulation patterns result in BBA-laden air flowing from the continent over the southeast Atlantic in the lower FT, then subsiding onto the semi-permanent stratocumulus cloud deck and entraining into the MBL. This study is broken into two parts, first analyzing hydrologic histories of the BBA air in the lower FT, and then carrying out a similar assessment in the underlying MBL. Both analyses~~**, although connections are made where relevant. Aircraft in-situ**~~ leverage joint measurements of ~~**total**~~ water concentration and its heavy isotope ~~**ratios to are used to assess of air parcel precipitation history. Subsequently, the isotopic fingerprint of precipitation influence is used to identify the prevalence of wet scavenging of black carbon aerosols. In situ**~~ ratio, interpreted in the previously established (q, δD) phase space framework.

For the lower FT analysis, in-situ observations (water concentration, water isotope ratios) in the lower FT are combined with satellite and MERRA-2 global reanalysis data into simple analytical models to constrain hydrologic histories ~~**of BBA laden air originating over Africa and flowing over the southeast Atlantic**~~. We find that even simple models are capable of detecting and constraining the primary processes at play~~.~~, e.g. distinguishing air masses that experienced moist convection and precipitation (likely over the continent) from those that underwent dry convection and turbulent mixing. Regression of the aircraft data onto a simple model of convective detrainment is used to develop a metric of total precipitation ~~**history. The** approach is supported by complementary analysis **using**~~for the in-situ measurements, then compared to an aerosol metric of black carbon scavenging also derived from the in-situ measurements (the ratio of black carbon to carbon monoxide ~~(~~, BC/CO). There is a strong correlation between the two, suggesting black carbon scavenging has been detected and partially quantified, if only in a relative manner. In comparison, weak correlation is found between BC/CO and the total water concentration itself.

The above method is expanded to test ~~**the**~~for entrainment and precipitation influences on ~~**marine boundary layer**~~

~~air.~~BBA concentrations in the MBL. This is more difficult than the ~~lower~~ FT analysis since signals are ~~more~~ subtle, and limited by imperfect knowledge of the water and isotope ratios of the entrained ~~airmass~~air mass at cloud-top. ~~Nonetheless~~For some of the MBL's observed during 2016 and 2018, lower cloud condensation nuclei (CCN) concentrations occur in the sub-cloud layer coincident with ~~isotope ratio~~isotopic evidence of precipitation, indicating aerosol scavenging ~~in the 2016 and 2018 IOPs.~~, but more complex models are needed to produce definitive conclusions. For the 2017 ~~IOP~~observation period, with the highest sub-cloud CCN concentrations, there is no connection between precipitation signals and CCN concentrations, likely indicating the importance of ~~the~~ different geographic sampling and air mass history in that year. ~~These~~Nonetheless, these findings ~~demonstrate the value of leveraging the~~ along with the FT analysis suggest that utilizing isotope ratio signals ~~of precipitation history that is distinct from the signature of dilution effects~~may be an aid in addressing cloud-aerosol challenges. Especially for the FT case, these findings support the pursuit of more complex models combined with targeted in-situ data to constrain BC scavenging coefficients in a manner which can guide ~~in~~ model parameterizations, ~~and ultimately lead~~leading to improvements in the accuracy of simulated BC concentrations and lifetimes in climate models.

1 Introduction

Cloud-aerosol interactions are primary sources of uncertainty in anthropogenic climate forcing (IPCC 2013). Biomass burning ~~(BB)~~ is a key source of aerosols (Bond et al., 2013), and central/southern Africa accounts for almost one third of ~~BB~~biomass burning emissions (550 TgC yr^{-1}; van der Werf et al., 2010). Black carbon (BC) is a component of African ~~BB~~biomass burning with potentially the strongest climate forcing effects. The atmospheric lifetime of BC determines its atmospheric burden and contribution to radiative impacts (Bond et al., 2013; Liu et al., 2020). Despite low hygroscopicity when initially formed, BC can serve as cloud condensation nuclei, particularly after ~~again~~aging (Zuberi et al., 2005; Zhang et al., 2008; Tritscher et al., 2011; Twohy et al., 2021). The main removal mechanism of BC is wet scavenging by clouds and precipitation (Latha et al., 2005; Textor et al 2006). Therefore, quantifying processes controlling BC scavenging efficiencies ~~are~~is of importance for climate models.

The ~~BB~~biomass burning aerosols (BBA) originating over central/south Africa are routinely transported across the South Atlantic basin (Chand et al., 2009; Zuidema et al., 2016) in the free troposphere (FT) at 2 – 6 km, and may subsequently subside and interact with the large, semi-permanent stratocumulus cloud deck in the Southeast Atlantic. One way aerosols could potentially change cloud cover is by altering cloud lifetimes (Albrecht, 1989; Ackerman et al., 2000; Wood 2007). For example, high aerosol loads may alter cloud droplet size distributions and suppress precipitation, in turn increasing cloud lifetimes. Both the magnitude and sign of the lifetime effect are not sufficiently constrained (Redemann et al., 2021; IPCC 2013).

~~A component of both~~ BC lifetimes in the atmosphere ~~and~~involve its interaction with precipitation, while cloud lifetime effects ~~is~~involve aerosol ~~interaction with~~modification of precipitation. Therefore, obtaining good observational constraints of the removal of water and aerosols by precipitation ~~relative~~compared to the reduction in concentrations due to dilution (e.g. turbulent mixing during convection or cloud-top entrainment) is important to constrain coincident behavior of clouds and aerosols. Measurements of the heavy ~~water~~stable isotope ratios of water vapor and total water concentrations provide a~~-~~ basis for a solution to these challenges, because they provide

information on the relative importance of the history of air mass mixing, precipitation, and other moisture transport processes that is not easy to determine from conventional thermodynamic variables alone (Galewsky and Hurley, 2010; Noone et al., 2011; Risi et al., 2012; Bailey et al., 2013; Benetti et al.., 2015; Steen-Larsen et al. 2015). WhilePrevious studies leveraging heavy water isotope ratio informationratios have been able to date has shown promise,partially but not fully constrain such processes. One reason for this is that the needed vertical profile information on isotopic compositions in the lower troposphere and the marine boundary layer (MBL) are limited. Therefore, an experimental design that integrates isotope ratio measurements paired directly with the complementary thermodynamic and aerosol measuresmeasurements is required to take full advantage of their tracer capacity and use for assessing aerosol cycling in the advantages to be realized. atmosphere.

The analysis presented here utilizes an extensive aircraft in-situ dataset taken during the NASA ORACLES (ObseRvations of Aerosols above CLouds and their intEractionS) campaign (Zuidema et. al., 2016; Redemann et. al., 2021). In addition to in-situ thermodynamic, trace gas, and aerosol variables, the dataset includes in-situ measurements of the isotopic compositions forheavy water D/H.stable isotope ratios. The campaign involved three, month-long sampling periods in the southeast Atlantic (SEA) FT and stratocumulus-topped marine boundary layer (SCMBL),MBL, targeted at sampling African BBA plumes and the SEA southeast Atlantic cloud deck. This study assesses both the FT and SCMBLMBL measurements to describe the mean atmospheric state and the interaction between distinct atmospheric layers. .. In the case of the FT, , regional aerosol and moisture transportthe hydrologic histories of high vs. low BBA air (assumed to have originated in the African planetary boundary layer) are connected and characterized (e.g. compared.Fig. 1a). The relative importance of evapotranspiration, dry versus moist convection, and precipitation (e.g. Fig. 1a) in controlling isotope signals of FTthese air originating over Africamasses are constrained primarily by interpreting the paired in-situ measurements of water concentration and water isotope ratios in (q, δD) phase space using previously established analytical models (e.g. Noone 2012).

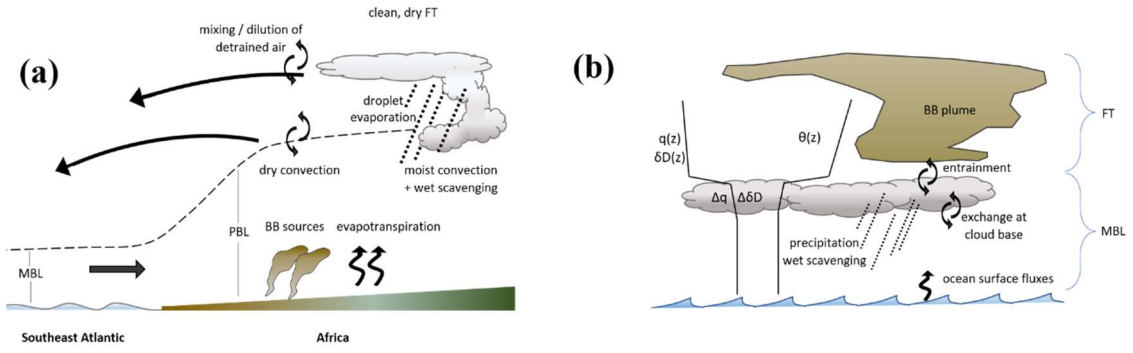

Figure 1. **(a) Regional moisture and aerosol transport associated with BBA plumes in the Central African and Southeast Atlantic regions before FT sampling during ORACLES. Processes expected to alter moisture, isotope ratios, and aerosol concentrations are shown. (b) Stratocumulus topped marine topped boundary layer schematic, showing relevant processes to this study. Characteristic potential temperature (θ), total water (q), and HDO/H_2O ratio (δD) profiles are included.**

~~constrained. Hydrologic histories of high versus low BBA loaded air masses are distinguished, and correlation between isotopic and aerosol is used as evidence that identifies wet scavenging.~~Regression of the isotope data onto a simple model of convective detrainment is used to develop a metric of total precipitation for the in-situ measurements, then compared to an aerosol metric of black carbon scavenging also derived from the in-situ measurements. Next, the occurrence of entrainment mixing and precipitation in the stratocumulus topped boundary layers is evaluated by ~~utilizing~~integrating the isotopic difference between sub-cloud layer (SCL) and cloud ~~layers.~~ layer (CL) into the (q, δD) phase space framework. Correlation between processes diagnosed with the isotope ratios and variation in ~~sub-cloud~~SCL aerosol abundance is also assessed. ~~Both the FT and SCMBL analyses leverage expectations for the relationships between the isotope ratios in relation to water concentration with simple analytical models as a diagnostic framework.~~

Section 2 covers the ORACLES sampling region, data, and basic isotope theory. Section 3 first presents ~~a brief analysis of the sub-cloud as a starting point for contrasting the analysis of~~ the FT analysis of precipitation histories and BC scavenging~~. Section 4 returns to~~, and then presents the case of the ~~SCMBL~~stratocumulus-topped MBL to test the degree to which the isotopic signals can detect recent precipitation ~~metrics can be applied to~~(e.g. before the signal is removed by subsequent boundary layer mixing) in that very different hydrological setting. Section 4 provides a discussion of the results and Section 5 provides final remarks ~~and conclusions~~.

2 Methods

2.1 ORACLES sampling region

An extensive overview of the ORACLES project is presented by Redemann et~~.~~ al., (2021~~)~~). Aspects of the project and ORACLES measurements relevant to this study are outlined here. In-situ sampling aboard the NASA P-3 Orion aircraft covered the southeast Atlantic MBL and ~~LCLT~~ lower FT during periods of high aerosol loading. The high BBA concentrations in the southern hemisphere spring are due to BBA-loaded air in the African ~~PBL~~planetary boundary layer being carried out over the ~~SEA~~southeast Atlantic by ~~LCLT~~ lower FT easterly flow (Garstang et al., 1996; Adebiyi and Zuidema, 2016). This air settles over the ~~SEA~~southeast Atlantic cloud deck due to large~~-~~scale subsidence, ~~where it~~and that air may then entrain into the MBL. The large-scale subsidence also plays a role in the strong inversion topped MBLs of the region~~; the MBLs~~, which transition to cumulus-coupled ~~SCMBLs~~MBLs toward the equator as sea surface temperatures (SSTs) increase (Wood 2012 and references therein).

Sampling flight tracks are shown in Figure 2. Sampling took place over three intensive observation periods (IOPs): Aug. 31 – Sept. 25, 2016 (14 flights); Aug. 12 – Sept. 2, 2017 (12 flights); and Sept. 27 – Oct 23, 2018 (13 flights). Flights were typically every 2-3 days~~. Most flights were~~, 7-9 hours in duration, and within 7am to 5:30pm local

time. Vertical profiles spanned the altitude range ~~100m~~100 m to ~~7km~~7 km, covering the MBL and the region of the FT where ~~BB~~biomass burning plumes were present.

2.2 P-3 variables used

Total water mixing ratio (q) and heavy isotope ratio $R_D = q_{HDO}/q_{H2O}$ were measured with the Water Isotope System for Precipitation and Entrainment Research (WISPER) instrument package, which centered around two Picarro isotopic gas analyzers (models L-2120fxi and L-2120i). The isotope ratios are reported in delta notation, the deviation of R_D from that of Vienna Standard Mean Ocean Water: ~~$\delta D \equiv (\delta D \equiv (R_D/R_{D,SMOW}$~~ - 1). A detailed description of those data and calibration methods is given by Henze et al.~~.~~, (2022). ~~Measurements of potential~~Potential temperature (θ) ~~were~~was computed from measurements of temperature (T, Rosemount 102 type non-deiced probe) and static and dynamic (ram) pressures. Refractory black carbon (rBC) and carbon monoxide (CO) are used as indicators of BBA loading in this study. rBC concentration from 53 to 524 nm mass equivalent diameter and adjusted to standard temperature and pressure was measured using a Droplet Measurement Technologies single-particle soot photometer (Stephens et al., 2003; Schwarz et al., 2006). CO concentrations were measured by an ABB–Los Gatos Research $CO/CO_2/H_2O$ analyzer (Liu et al., 2017). Cloud condensation nuclei (CCN) concentrations at 0.3% supersaturation were measured by a Droplet Measurement Technologies CCN-100 continuous-flow streamwise thermal-gradient CCN chamber (Roberts and Nenes, 2005). Sub-cloud CCN measurements were used to estimate the total amount of hygroscopic aerosols present in sampled MBLs. Measurements for q, δD, rBC, and CCN were sampled from a forward-facing solid diffuser inlet outside the P-3 cabin in front of the wing (McNaughton et al., 2007), operated by the Hawaii Group for Environmental Aerosol Research and maintained at near isokinetic flow. CO measurements were made from a rear facing Rosemount inlet probe.

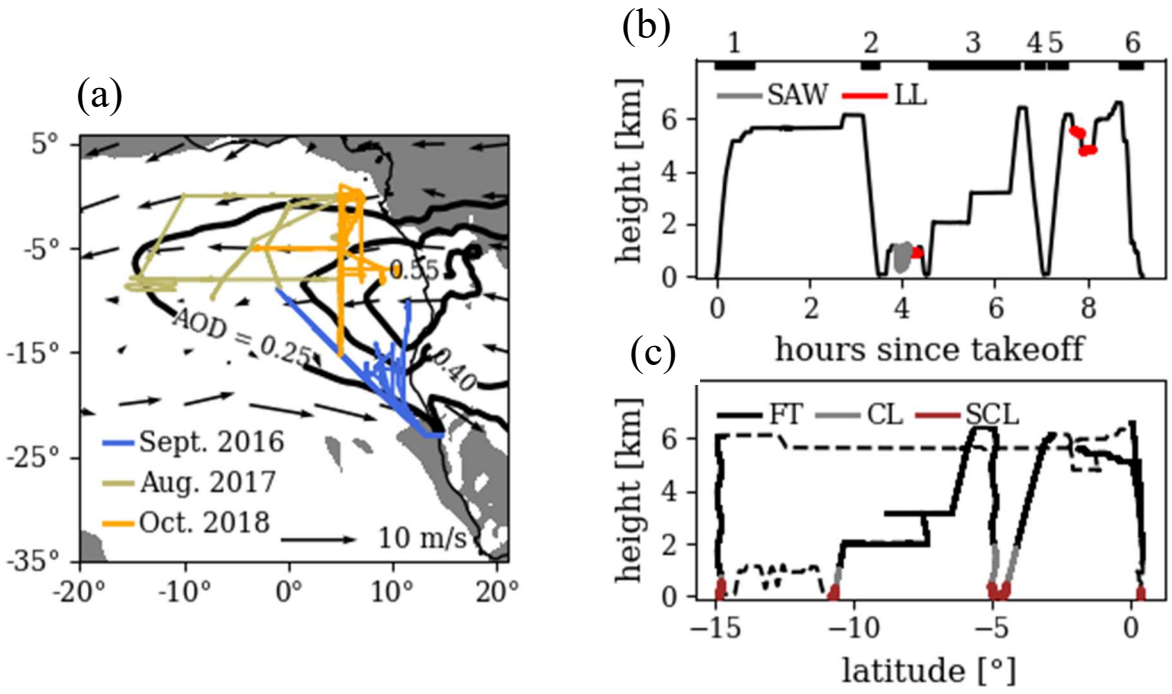

Figure 2. (a) ORACLES P-3 Orion flight tracks for the three IOPs. The majority of the 2017 and 2018 IOP flight tracks are co-located geographically (blue north-south track near lon 5W). The Sept. 2016 MERRA monthly mean aerosol optical depth (black contours) and 500 hPa winds (arrows) between latitudes 25°S and 8°N are shown. Shading indicates where the Sept. 2016 MERRA monthly mean 500 hPa vertical velocity is upwards. Aerosol optical depth, 500 hPa winds, and 500 hPa vertical velocity are qualitatively similar for the Aug. 2017 and Oct. 2018 observation periods. (b) P-3 height vs. time for the flight on Aug. 24, 2017. In-cloud level legs (red) and sawtooth patterns (~~grey~~gray) are highlighted. Black bars with numbers on top indicate manually identified vertical profiles. (c): P-3 height vs. latitude, with SCL, CL, and FT regions distinguished using the vertical profiles in the top panel and the methods in Section 2.3.

2.3 SCL, CL, and FT identification in vertical profiles

For each flight, time intervals of vertical profiles were flagged manually. To maximize the amount of data used in this study, profiles were liberally identified as any flight segment with a progressively upward or downward trajectory from near the surface (100 – 200 m) to at least 2500 m (e.g. Fig. 2). For each profile, vertical profiles of T, θ, and relative humidity (RH) averaged into 50 m vertical bins were used to identify the well-mixed layer top and MBL capping inversion bottom as described below. Data below the well-mixed layer top are flagged as SCL, data between mixed layer top and inversion bottom are flagged as ~~cloud layers (~~CL~~),~~, and data above the inversion ~~bottom~~ are flagged as FT. ~~Using vertical~~For the FT analysis, it was desired to highlight hydrologic histories of distinct air masses from the African continent (e.g. different BBA plumes), rather than any subsequent mixing between them as they advect westward to the southeast Atlantic. Therefore, once FT segments of each profile were identified, the portions of those segments determined to be distinct air masses were isolated (rather than intermediary mixtures between them) and used for the analysis in Section 3.2. This was done using a pseudo-conservative variable approach described in Appendix B.

Vertical profiles of T, θ, and RH ~~was~~were chosen over liquid water content ~~as a~~to flag ~~for~~ the CL since ~~it~~the algorithm would also capture profiles through CLs with broken clouds, where by chance the P-3 avoided clouds during vertical ascent or descent.

Mixed layer tops were roughly taken to be the height at which ~~potential temperature~~θ increased by 0.2 K from its 100 – 300 m mean. A potentially more rigorous identification of cloud-base using lifting condensation levels was not used since data below 100 m was not always available. The MBLs in the study region were almost always characterized by a capping temperature inversion and a peak in RH at their top. Inversion bottoms were identified as the highest altitude below 2.5 km where a temperature minimum coincided with an RH maximum to within 150 m. The temperature minimum relative peak had to be at least 1 K and occur within a vertical region of 400 m or less. The RH absolute peak had to be greater than 80% and occur within a vertical region of 300 m or less. Figure 2 shows an example flight using the above methods to identify SCL, CL, and FT. Using this method, the majority of data are flagged as one of the three regions and are able to be used for analysis.

2.4 Cloud layer modules

Most flights involved modules to directly target the CL. These included: (1) level legs through the cloud layer at a single altitude (LLs), typically lasting 5 – 15 minutes, (2) sawtooth patterns through cloud layer (SAWs), also typically 5 – 15 minutes, where individual saw teeth spanned the full vertical extent of the cloud layer (Fig. 2). Both LL and SAW modules were previously flagged (~~Redemann et al., 2021) as used in~~e.g. Diamond et al., 2018~~.~~). Where available, these modules are preferred over the CL flagging in Section 2.3. For LLs, data were averaged into 3-minute blocks. At an aircraft horizontal speed of 130 m s^{-1}, each block represents almost 25 km of horizontal distance, ~~equivalent to~~which is half the horizontal grid spacing ~~of~~for higher resolution GCM simulations. SAW patterns included periodic portions above and below the CL. To ensure only the CL portioned are used, times where RH drops below 99% are discarded. The remaining data are averaged into 3-minute blocks. Only LLs and SAWs below 2.5 km are used.

2.5 ~~Identifying distinct FT airmasses~~

~~Distinct FT airmasses in each vertical profile were identified using a pseudo-conservative variable approach to highlight the differing hydrologic histories rather than the subsequent mixtures between them. Simple two-endmember mixing processes are found as straight lines on the diagram while curved segments signal non-conservative processes such as precipitation, or more complex mixing environments (such as multiple sources or time evolving end members). Diagrams of q vs equivalent potential temperature (θ_e) have been used before to identify regions of mixing in atmospheric profiles as well as the mixing endmembers (Paluch, 1979; Betts and Albrecht, 1987). Here, instead of θ_e, the quantity $q\delta D = q_{HDO}/R_{D,SMOW} - q$ is utilized (since the mixing ratios q_{HDO} and q are both conserved in mixing processes, so is the linear combination q δD).~~

~~P-3 vertical profiles as identified in Section 2.3 were averaged into 25m altitude bins and their trajectories in *q* vs *qδ*D space were visually broken into piecewise segments.~~ ~~Figure 3 shows an example of segment identification, with associated profiles of thermodynamic quantities and the BBA indicator rBC. The diagram of *q* vs *qδD* shows a series of piecewise segments, where the corners/kinks are taken as the independent endmembers (open circles). The vertical profiles show that these air masses correspond to minima/maxima in the profiles of *q*, *δD*, and rBC, or are near kinks in the *θ* profile, supporting the validity of this method. Although some of these airmasses reside in the MBL, only the FT airmasses were used.~~

~~2.6~~ Analysis of ~~airmass~~air mass hydrologic histories using humidity-isotope pairs

The *δD* of an air mass relative to its water vapor mixing ratio, *q*, will assume different relationships depending on the hydrologic processes the air mass experiences. PDFs in (*q, δ*D) space can be compared to theoretical curves (e.g. Figure 3) to constrain these processes. A survey discussion on the theory is presented in Noone (2012) (note that "*q*" in Noone 2012 denotes water vapor while here denotes total water). Some key components are presented here to facilitate discussion below.

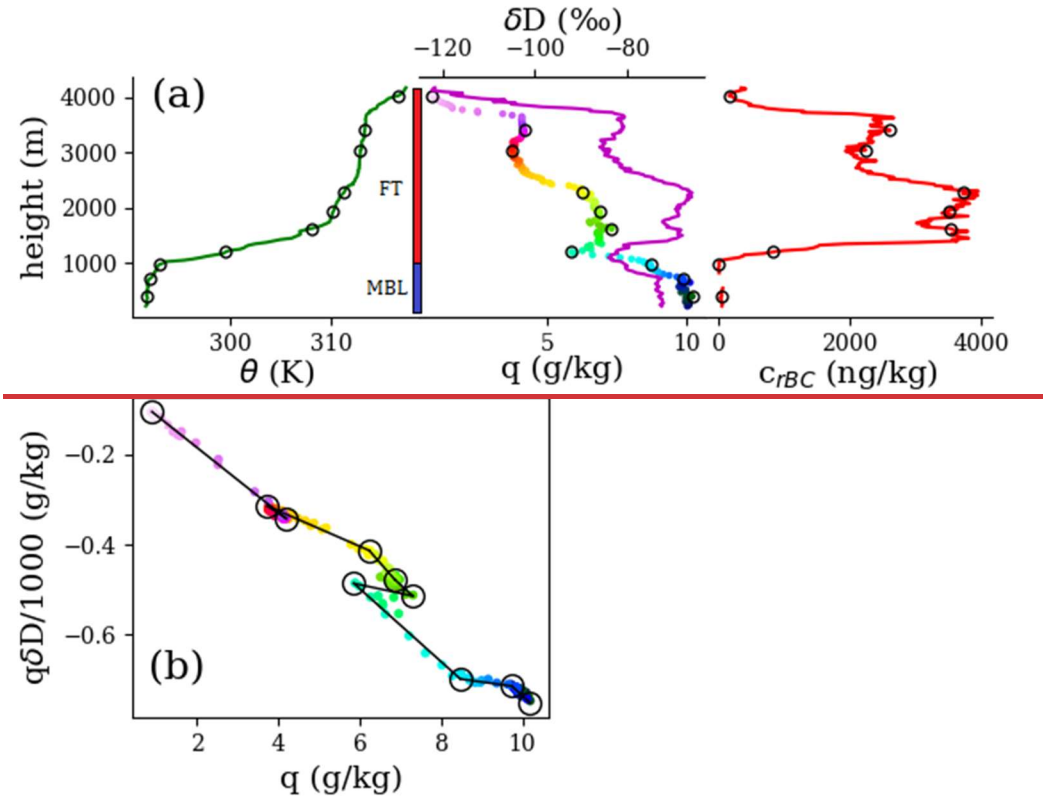

~~**Figure 3.**~~Figure 3 shows the (*q, δ*D) value of asymptotic end members for dry FT ~~**(a) One of the P-3 vertical profiles on the Sept. 4, 2016 flight, averaged into 25m bins. Profiles of in-situ potential temperature (green), total water mixing ratio (multi-color), δD (magenta), and refractory black carbon (red). (b) q vs. qδD for the profile, with the same altitude-**~~

~~coloring as the total water profile. Open circles in (a) and (b) mark distinct air masses as outlined in Sect. 3.3.5, identified visually from (b).~~

~~Figure 4 shows the (*q, δD*) value of an asymptotic endmembers for dry free tropospheric (FT)~~ air and pure surface evaporation from land and ocean sources. Land surface evapotranspiration (ET) may have higher δD values than ocean evaporation since transpiration does not fractionate heavy isotopes. The mixing trajectories (black, ~~grey~~gray) show the (*q,* δD) relationship for air where moisture from the respective evaporation source ~~and~~ is diluted with FT air to varying degrees. In general, air that has not experienced condensation processes may be ~~modelled~~modeled as a mixture of two or all of these ~~endmembers~~end members. The blue circle in Figure 3 shows an example MBL placement on the mixing line assuming 80% relative humidity with respect to a sea surface temperature of 293K~~.~~ (alternatively, the blue circle could represent planetary boundary layer air over the African continent). Further entrainment of FT air into the ~~marine boundary layer~~MBL (or conversely detrainment of MBL air into the FT) would continue along the mixing trajectory. On the other hand, precipitation preferentially removes heavy isotopes, resulting in a steeper trajectory. The black-dashed curve in Figure 43 shows the extreme case of 100% condensate removal (Rayleigh process).

~~Air that experiences either condensate removal at less than 100% efficiency or a combination of precipitation and mixing will fall between the grey solid and black dashed curves. If we assume a simple convective plume model with no entrainment, a convecting airmass~~In the absence of rain droplet re-evaporation, the mixing and Rayleigh processes are limiting cases that bound the region of (*q,* δD) space in which we expect measurements to lie. If data lie directly on the mixing curve, we hypothesize that mixing was the primary process in the recent history of the sampled air (and likewise for Rayleigh). If data lie between the curves, then the air has a more complex history. In this study, we assume that the most frequent hydrologic history occurring for the BBA-laden air is that of a convective plume model with no entrainment and 100 % precipitation efficiency (e.g. Rayleigh), which detrains at various altitudes. A convecting air mass undergoing a Rayleigh process would first follow the dashed curve from the blue circle, but then divert along the 'convective detrainment' mixing curve (solid line) upon reaching a detrainment level, when the air mass begins to dilute with FT air. ~~In~~We use this ~~study,~~model to estimate total precipitation amounts in sampled FT air based on their in-situ (*q,* δD) values (as described further in Section 3.3 and Figure 9).

To support our use of the above convective detraining plume, we also compare temperature and altitude measurements from the P-3 to detrainment ~~heights~~altitudes and temperatures ~~are estimated along the Rayleigh trajectory as an estimate of detrained water, and is not substantially different from a partial removal model (e.g., Merlivat and Jouzel, 1979, Noone 2012) at high water vapor mixing ratios.~~estimated from the in-situ (*q,* δD) and our model (Section 3.2). The algorithm used has the following features (1) Values of surface *q, T* and elevation (e.g. starting values for air lying at the blue circle in Fig, 4) are estimated from MERRA reanalysis and used as initial conditions. (2) A temperature profile is computed from these surface values, assuming a dry adiabatic lapse rate up to a lifting condensation level ~~(LCL)~~ and a moist lapse rate above ~~the LCL~~. (3) For each q value along the Rayleigh

trajectory, a dewpoint is calculated as the detrainment temperature and the height at which the dew point intersects the temperature profile is the detrainment height. Figure 43 shows a characteristic case with the dew point and height from this computation for the example MBL undergoing convection and detraining at q = 6 g kg^{-1}.

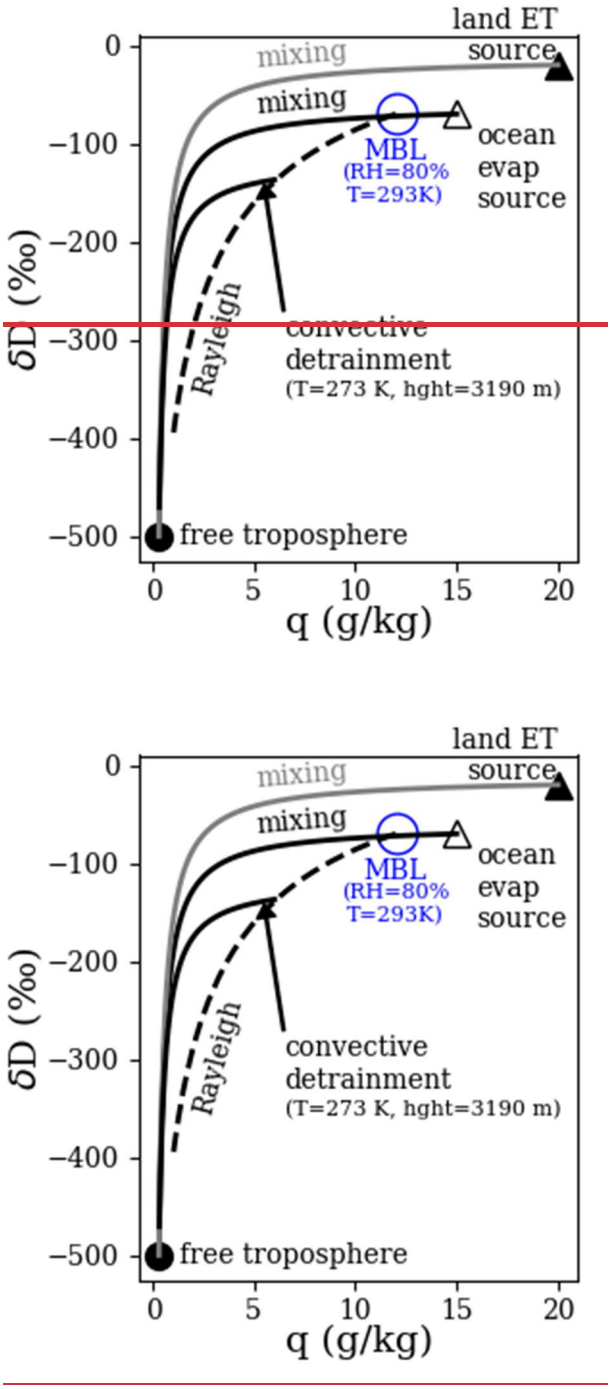

Figure 43. Theoretical trajectories in (q, δD) space. Equations to generate curves were taken from Noone 2012.

3 Results

~~3.1 Sub-cloud layer humidity and δD variance~~

~~Figure 5 shows of~~**3.1** ~~SCL data averaged into 60-s blocks, where the SCL was identified as in Sect. 3.3.3. Data below 150 m are colored by SST. SST was determined by collocating NOAA COBE monthly mean SST satellite data with the position of the aircraft. Previous studies have been devoted to a detailed understanding of the isotopic composition of the SCL, typically using either land or ship-based measurements (e.g. Benetti et al., 2018; Feng et al., 2019). Rather than testing those analyses in detail, the ORACLES SCL data are shown here briefly for context as a basis for the novel aspects of the aircraft profile dataset. Nonetheless, Figure 5 includes *δD* predictions using the simple model of Merlivat and Jouzel, 1979 (MJ79). The MJ79 model – which assumes SCL moisture comes solely from ocean evaporation – was not originally intended for regional scale and sub-daily predictions and its limitations in doing so have been investigated elsewhere (e.g. Jouzel and Koster, 1996; Kurita, 2013). The MJ79 model reduces SCL *δD* to a simple function of SST and relative humidity with respect to SST (*RHS*), and provides a useful reference point. For each 60-s average, the MJ79 formula was used for ocean *δD* values in the range of -0 ‰ to 6 ‰ for the 2017 and 2018 IOPs, and in the range 0 ‰ to 10 ‰ for 2016. The range was used to account for uncertainty in the ocean isotopic values which were not sampled during ORACLES. The upper bounds were taken by inspection of Fig. 4 in Benetti et al. (2017).~~

~~The right column of Fig. 5 provides a metric of variability in the SCL. The histograms show the difference between means of the lower and upper most sampled 100 m of the SCL for each vertical profile in Section 2.3. The standard vertical difference is about 1 ‰ for 2016 and 2 ‰ for the other two IOPs. Horizontal variability is also explored. Horizontal aircraft legs below 500 m and lasting at least 3 minutes were averaged into 10-s blocks and then the standard deviation of the entire leg was computed. The median horizontal standard deviations are roughly the same as the standard vertical variabilities for 2016 and 2017. For 2018, the median horizontal variability is 1.25 ‰, slightly less than the 2 ‰ vertical variability.~~

~~3.2~~ FT rainfall and evapotranspiration histories from satellite data

One objective of this study is to build a characterization of rainfall and evapotranspiration histories for FT air sampled during ORACLES using the humidity and isotopic data. For comparison, a characterization using ~~airmass~~air mass back-trajectories and satellite products of monthly mean rainfall and evapotranspiration is also developed. ~~Figure 6 shows six-day back-trajectories~~The goal of this additional characterization is to provide a rough idea of the relative differences in precipitation and evapotranspiration which air experienced (on average) across sampling periods and across BBA concentrations. For this, six-day back-trajectories were computed with HYSPLIT (Draxler and Hess, 1997, Warner, 2018) via the PySplit Python module (Warner, 2018) for FT ~~airmasses~~air masses sampled by the P-3 (HYSPLIT runs used Global Data Assimilation System output on pressure levels at 1˚ x 1˚

resolution and 3-hour frequency~~). The~~, and outputs air parcel positions at 1-hour frequency). Figure 4 shows the trajectories ~~are~~ separated by sampling period and BBA loading histories inferred from their in-situ CO concentrations. ~~Airmasses~~Air masses where the in-situ CO concentrations were higher vs. lower than the FT median for that sampling period are referred to hereafter as high-BBA vs. low-BBA ~~are~~, respectively. It is noteworthy that a large fraction of the "low-BBA" ~~can have~~air in the FT had CO concentrations double that ~~of~~typically measured in the SCL ~~(Fig. 6c).~~ during the campaign (not shown).

For 2016, high-BBA originates from the highest latitudes out of the three years. For 2017, both high-BBA and low-BBA air originate further north and their latitudes tend to overlap. For 2018, the low-BBA trajectories are on average displaced 3˚ north of the high-BBA trajectories, toward regions of higher rainfall. The high-BBA air originates from a region similar to that of 2016 but whereas the 2016 high-BBA air flows west off the continent, the 2018 high-BBA air tends to flow north-west. The low-BBA air in 2016 ~~it~~ is distinct as it often originated from higher latitudes of the Atlantic Ocean.

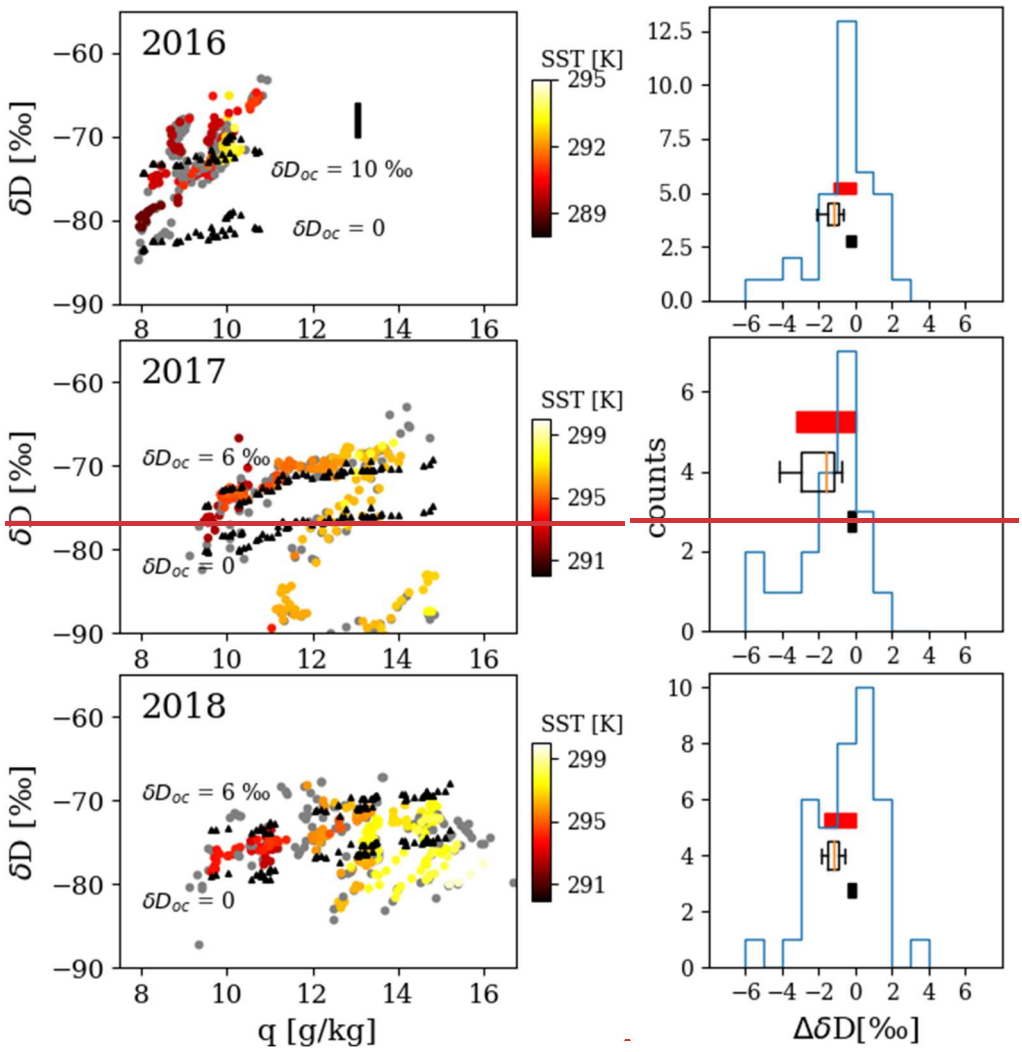
2016
2017
2018
δD [‰]
q [g/kg]
SST [K]
δD_{oc} = 10 ‰
δD_{oc} = 6 ‰
δD_{oc} = 0
counts
ΔδD[‰]

~~Figure 5.~~

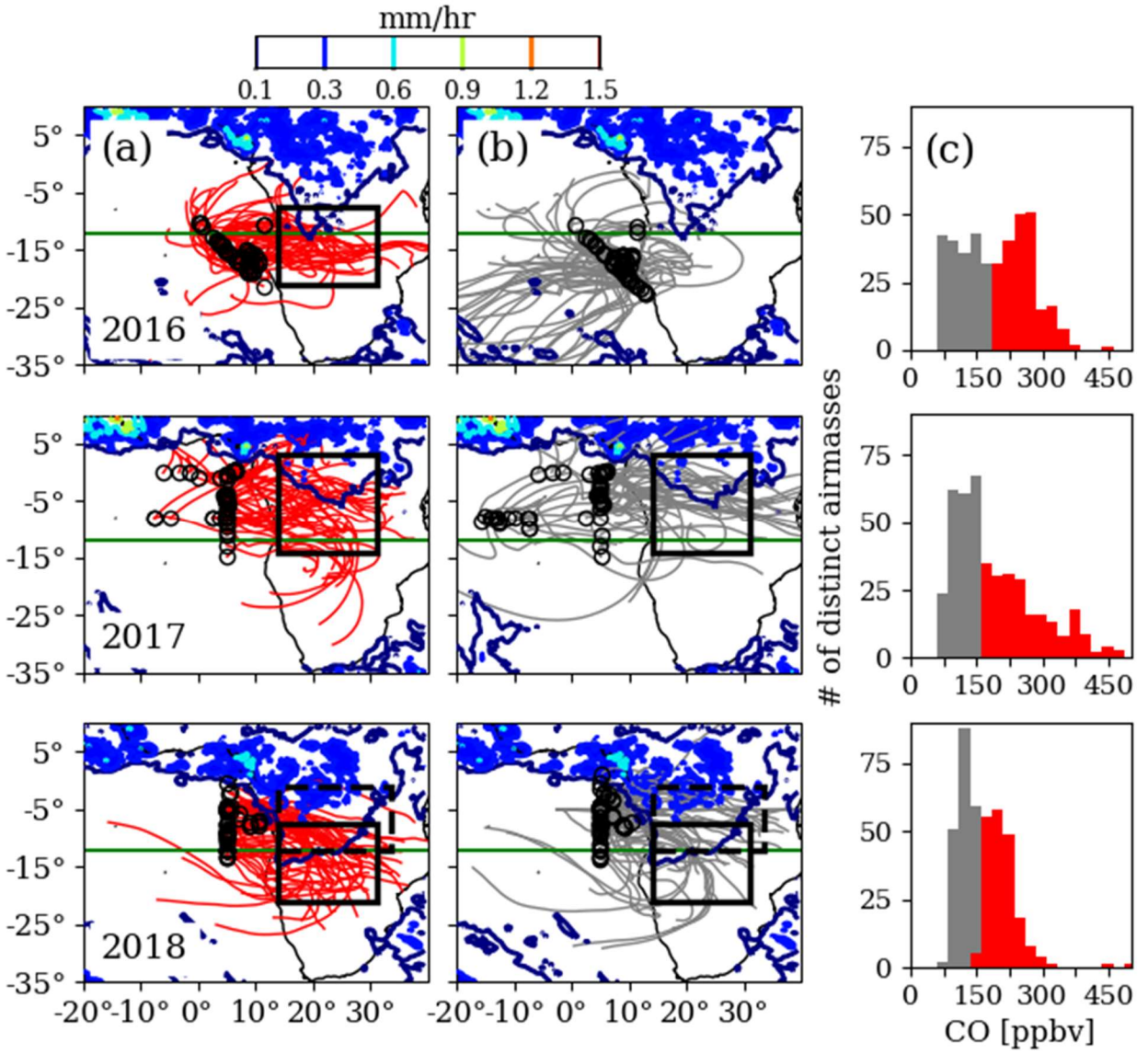

Figure 4. HYSPLIT back-trajectories for distinct FT air masses (identified using the methods in Appendix B ~~(Left column) (*q*, *δD*) data in the SCL for 2016 (top), 2017 (middle), and 2018 (bottom), averaged into 60 s blocks. Measurements below 150 m height are colored by NOAA COBE monthly mean satellite SST. Black triangles show predictions using the Merlivat and Jouzel (1979) closure assumption. The vertical black bar displayed for 2016 is the instrument standard error on an absolute scale. (Right column) Histograms of the difference in *δD* between the top and bottom most sampled 100 m of the SCL for each vertical profile. Red bars are the standard deviations of the histograms. Box plots are the *δD* standard deviations of all P-3 horizontal legs below 500 m height and lasting at least 3 min averaged to 0.1 Hz (n = 23, 22, 25 for 2016, 17, 18 IOPs). Black bars are 0.1 Hz instrument precisions. All standard deviations are multiplied by -1 for visuals.~~

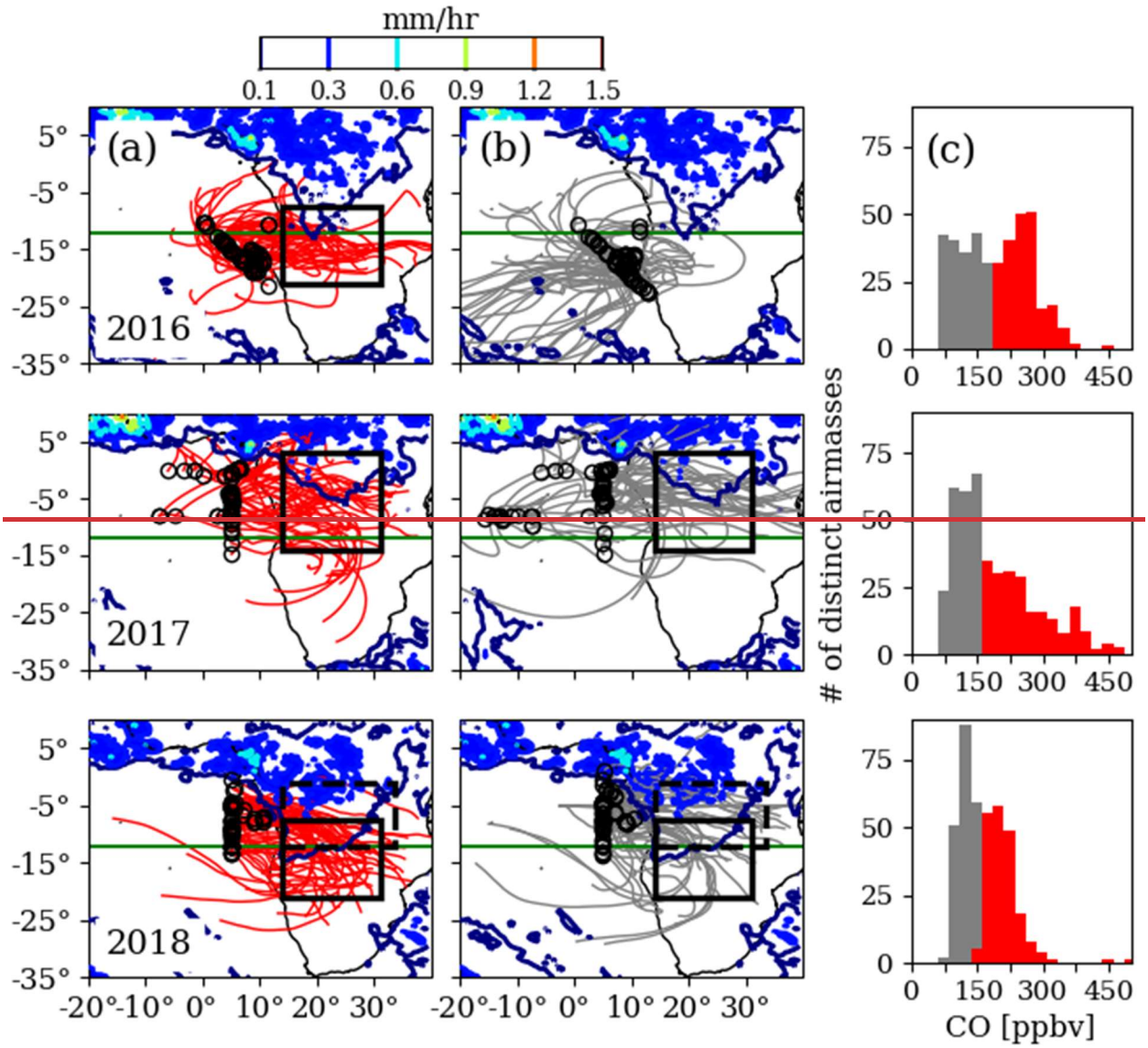

~~Figure 6. HYSPLIT back-trajectories for distinct FT airmasses (identified using the methods in section 2.5~~) with in-situ CO greater than the median (a) vs. less than the median (b). CO histograms are also shown (c). Back-trajectories are shown for the Sept. 2016 (top row), Aug. 2017 (middle) and Oct. 2018 (bottom) IOPs. Black open circles mark trajectory end points - the locations of P-3 in-situ sampling. Overlain are NASA GPM satellite monthly mean rainfall maps for Sept. 2016, Aug. 2017, and Oct. 2018. Boxed regions mark areas over which mean MERRA and CAM values were taken for calculations discussed in the main text and outlined in Table ~~3.3~~2. The green line at 12°S is a visual reference. Median FT CO values for the 2016, 2017 and 2018 sampling periods were 200, 162, and 157 ppbv.

~~Across sampling periods there are distinct differences in the back-trajectory collocation with rainfall (Fig. 6). Fig. 7 shows that in~~Figure 5 provides a first coarse assessment of the possibility of precipitation formation underway across the air mass groups in Fig. 4. It shows PDFs of monthly mean rainfall values along the back-trajectories for each group, and distinct differences are apparent. In 2016, high-BBA trajectories show the lowest monthly-mean rainfall. The frequency along 2016 trajectories where satellite GPM monthly mean precipitation rates are greater than 0.25 mm hr^{-1} is an order of magnitude less than that for the other two years. For 2017, there is no significant difference in the PDFs for high-BBA vs low-BBA, while in 2018 the low-BBA trajectories are 2-3x

more likely than high-BBA to pass over regions with precipitation > 0.25 mm hr^{-1}. As will be shown further below, this characterization aligns with conclusions drawn from the isotope analysis. However, two sources of uncertainty in this first characterization are acknowledged: first, it is not clear if precipitation did really form at the time of the air mass overpass over a given region; and 2) it is not clear if the air mass being tracked is really the one involved in precipitation formation.

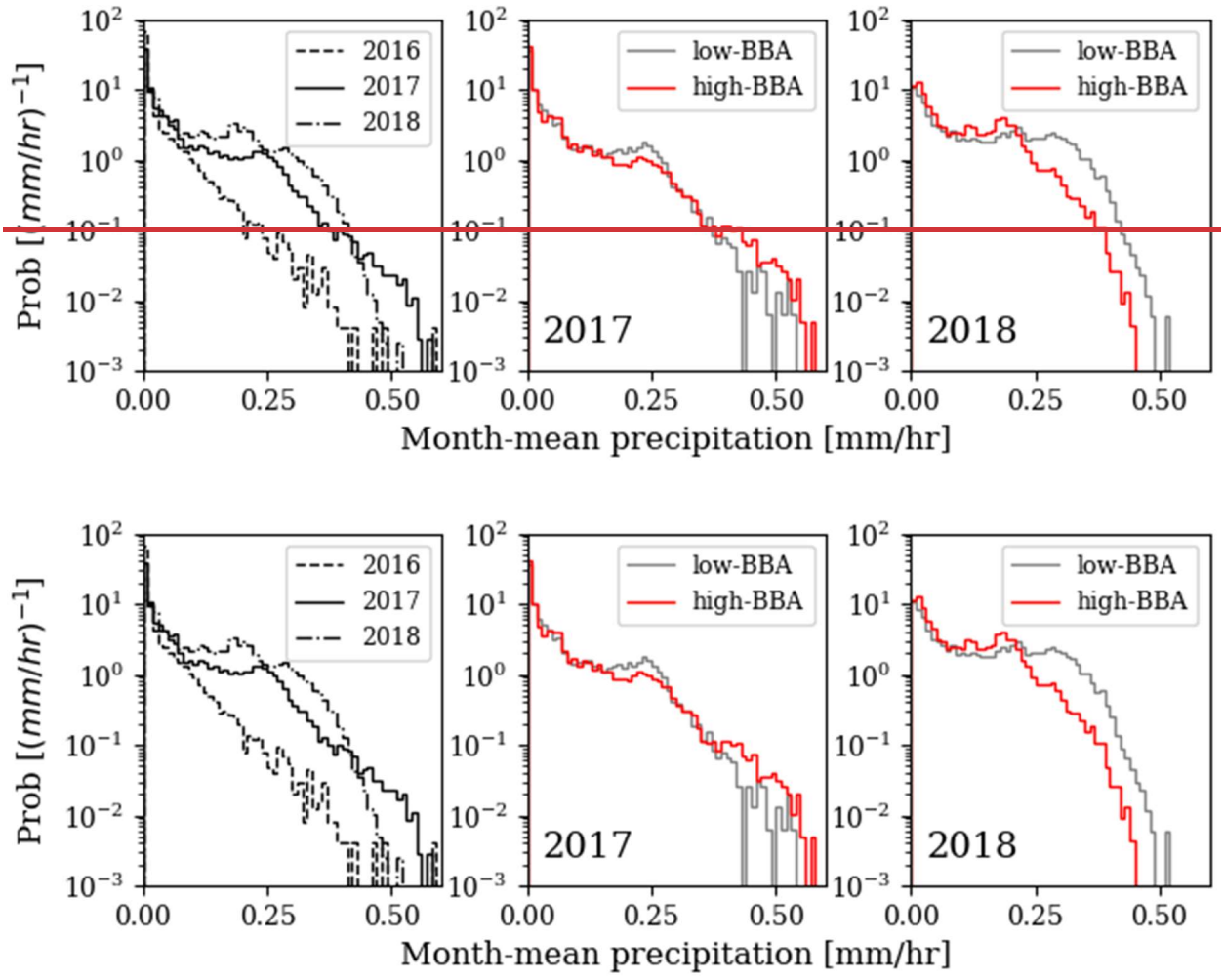

Figure ~~7~~5. Probability distributions of GPM monthly mean rainfall along FT back-trajectories in Fig. ~~6~~4. Only the portions of the trajectories over the African continent were used, defined roughly as any portion of the trajectory east of 10˚E. Distributions between IOPs are compared (left), and between high vs. low BBA air for the 2017 IOP (middle) and 2018 IOP (right).

Table 1. Estimated ET contribution to African ~~PBL~~planetary boundary layer moisture for each ORACLES sampling period, using a back of the envelope calculation (Appendix A).

Fig. ~~6~~4 Region	MOD16A2 mean ET (kg m^{-2} s^{-1})	Parameter Values	Δt (days)	% ET contribution
2016	$6 \cdot 10^{-6}$	h = 700 m,	1	6% (±4%)

solid box	($\pm 6 \cdot 10^{-6}$)	q = 9 g kg^{-1}, ρ = 1.2 kg m^{-3}	2	12% (±7%)
			3	17% (±10%)
2017 solid box	$3 \cdot 10^{-5}$ ($\pm 1.2 \cdot 10^{-5}$)	h = 1000 m, q = 12 g kg^{-1}, ρ = 1.2 kg m^{-3}	1	14% (±5%)
			2	25% (±7%)
			3	33% (±9%)
2018 solid box	$1 \cdot 10^{-5}$ ($\pm 1 \cdot 10^{-5}$)	h = 1000m, q = 12 g kg^{-1}, ρ = 1.2 kg m^{-3}	1	5% (±5%)
			2	10% (±7%)
			3	15% (±9%)
2018 dashed box	$3.5 \cdot 10^{-5}$ ($\pm 1.1 \cdot 10^{-5}$)	h = 1000m, q = 12 g kg^{-1}, ρ = 1.2 kg m^{-3}	1	16% (±5%)
			2	28% (±7%)
			3	37% (±8%)

In addition to precipitation, there is variation in mean evapotranspiration (ET) in the regions from which the trajectories originate. Because ET contribution can alter the isotopic content of an ~~airmass~~air mass, its expected fraction of moisture contribution for each sampling period was estimated using a back of the ~~envelope~~envelope calculation outlined in Appendix A~~.1~~ and the MODIS/TERRA Version 6 Evapotranspiration/Latent Heat Flux product (MOD16A2), taking the mean and standard deviation over the boxed regions (regions bound by black/dashed squares) of Fig. ~~6~~4. The results are shown in Table 3.1 and show expected ET contributions of roughly 5-15% at higher latitudes and 15-30% for central Africa.

3.~~3~~2 FT rainfall and evapotranspiration histories from in-situ humidity and isotope ratio analysis

The grouping scheme in Section 3.~~2~~1 (by IOP and BBA loading history) is used to categorize the in-situ data to determine if similar distinctions in their precipitation and evapotranspiration histories are derived using a (q-, δD) space analysis (Figures 6-8~~-10~~). The asymptotic ~~endmembers~~end members and theoretical curves reviewed in Section 2.~~6~~5 are estimated and plotted in Figures ~~8, 9~~6, 7, and ~~10~~8 for each sampling period. The symbols/curves for each quantity/process match those used in Fig. 4. Table ~~3.~~2 summarizes their computation. Some of the ~~endmembers~~end members require estimations of near surface values over either the ocean or African continent, as detailed in Table ~~3.~~2. Near-surface temperatures and water mixing ratios were estimated using monthly mean ~~10m~~10 m values from the Modern-Era Retrospective analysis for Research and Applications, Version 2 (MERRA-2). The δD of near-surface air over Africa is taken from output of the isotopic version of the Community Atmospheric Model simulations (isoCAM5, Nusbaumer et al., 2017) which were run for the ORACLES time period (2016-2018) and nudged with the MERRA-2 winds in a configuration very similar to that described by Fiorella et al., (~~2022~~2021). FT air masses are split into high-BBA (red) vs. low-BBA (~~grey~~gray) as in Section 3.~~2~~1. Data for high-BBA vs. low-BBA air in figures 6-8~~-10~~ are plotted as joint probability distributions (PDFs) of (q, δD~~. PDFs were~~), derived using a gaussian kernel density estimation. ~~The kernel bandwidth was estimated using Silverman's rule of thumb with a fudge factor of ¾ to account for over-smoothing.~~ SCL data are plotted in blue after 60 s averaging.

Horizontally, the SCL data on average fall between 65-80 % *RH* with respect to mean SST, which is reasonable. A further comparison of the SCL data with theory is provided in Appendix C. In short, the agreement between the measurements and simple theory is robust enough to provide an anchor point for the measurements and the analyses which utilize them.

The blue mixing curves in ~~figures~~ Figures 6-8 ~~10~~ use a combination of ORACLES in-situ and MERRA datasets along with the evapotranspiration estimations to provide more observationally constrained moist mixing ~~endmembers~~end members. For the 2016 IOP where ET is thought to be minimal, the mixing curve simply starts at the mean SCL (*q, δ*D) values. For the 2017 IOP, ET contribution is estimated as 25 %. The open box in Fig. ~~9~~7 represents a 75 % / 25 % mixture of mean ORACLES SCL and a (*q, δ*D) point taken from mean 10 m values derived from MERRA and isoCAM5 simulations 10 m over the boxed region in Fig. ~~6~~4 for 2017. It is taken as the moist ~~endmember~~end member for the blue curve. The dashed boxed in Fig. ~~10~~8 for the 2018 IOP is an analogous 75 % / 25 % mixture for the dashed box in Fig. ~~6~~4. The solid box is provided mostly for reference and is the point along the blue curve where q reaches its MERRA 10 m value over the solid 2018 box in Fig. 4.

Table 2. Methods for computing theoretical asymptotic ~~endmembers~~end members and curves for figures ~~8, 9~~6, 7, and ~~10~~8.

~~Endmember~~end member/ Process	Symbol/ line	Calculation
Ocean evaporation source	open triangle	Estimated as air in thermodynamic/isotopic equilibrium with the mean SST over each sampling period/region. SSTs were taken from the NOAA COBE monthly mean product. Isotopic equilibrium was computed using e.g. Noone 2012 equation 6, where equilibrium fractionation factors were computed from formulas in Horita and Wesolowski, (1994~~.~~). δD of the ocean water was taken as 3 ‰.
Continental ET source	filled triangle (runs off figures)	*q* was taken as saturation with respect to mean MERRA-2 surface skin temperature in the boxed region of Fig. ~~9~~7 for the respective sampling period. *δD* was taken as the mean *δD* surface flux from isoCAM over respective boxed regions.
Dry FT air	filled circle	Mean of all ORACLES WISPER in-situ data between 0.25-0.5 g kg^{-1}. Whiskers are standard deviations.
Mixing of FT air with ocean or land source	solid black and grey curves	Computed with Noone 2012, equation 23. Only a portion of the curves are shown in Figures 6 – 8~~—10~~.
Rayleigh (100% condensate removal)	dashed black curve	Rayleigh model (e.g. Craig et al~~.~~., 1963; Dansgaard, 1964). Starting point for each Rayleigh model is given in the respective figure caption.
T_{sat} & height along Rayleigh curve	arrows with annotations	As described in the last paragraph of Section 2.~~6~~5. Near surface T, q, and z for estimating the ~~LCL~~lifting condensation level were taken as mean MERRA-2 10 m temperature, 2 m

humidity, and surface elevation in the boxed regions of Fig. ~~6~~4.

While the majority of 2016 high-BBA data can be described by dilution of high humidity continental air with clean FT air (the blue mixing curve), the 2017 data fall well below this curve and require more analysis. ~~One possibility~~The assumed model here is a detraining convective ~~detrainment~~plume discussed in Section 2.5. Assuming an ascending parcel model following a Rayleigh process, q and δD would fall monotonically with height as water in the parcel condensed and precipitated out. Detrained air at a specific height would have a characteristic δD and subsequent mixing with ambient dry air would alter δD relatively little (by less than 20 ‰ until the air reached about 2 g kg^{-1} humidity ~~(e.g.)~~. If Rayleigh distillation followed by detrainment into dry air is in fact the ~~'detrainment' curves in Fig. 9).~~primary process for the 2017 air parcels, one expectation is that δD and altitude would have good correlation. For the 2017 IOP, a correlation of -0.67 is found between δD and altitude, with δD decreasing at a mean rate of -35 ‰ km^{-1}. In comparison, 0.05 correlation is found for the 2016 IOP despite similar sampling altitudes. Further, using the method outlined in Section 2.~~6~~5, detrainment heights and temperatures from the Rayleigh trajectory are estimated. The best fit lines (r of 0.68 for each) have slopes of 0.54 (Fig. ~~9~~7).

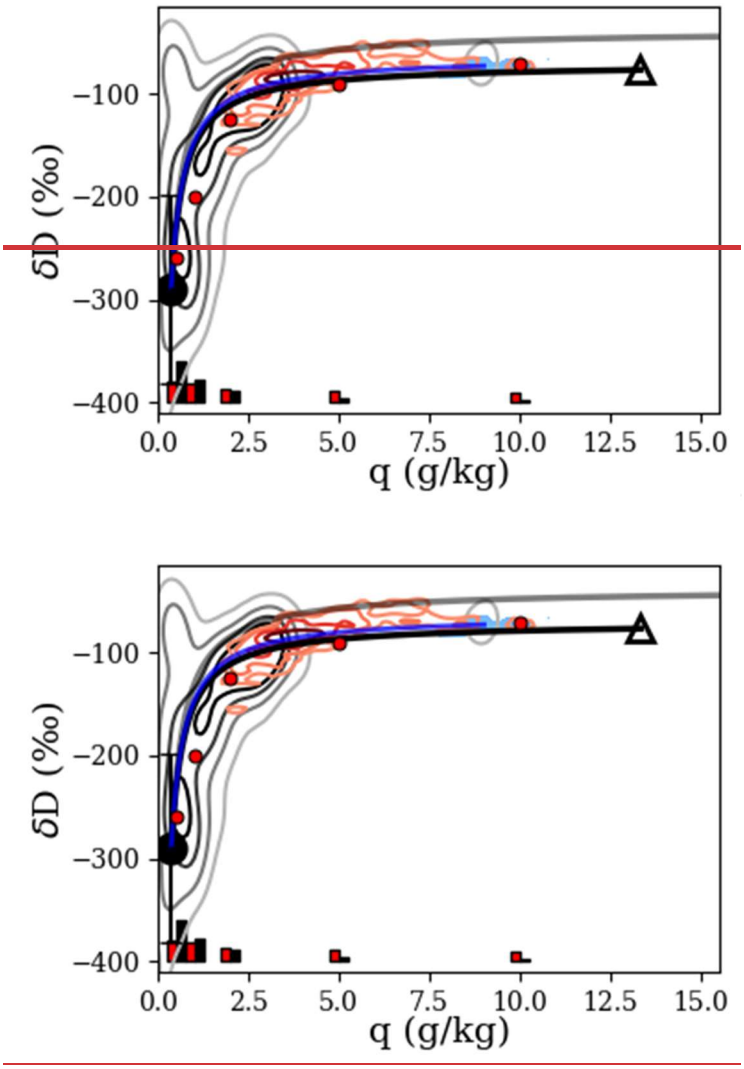

Figure ~~8~~6. (*q*, *δ*D) PDFs for distinct FT ~~airmasses~~air masses identified from vertical profiles during the Sept. 2016 sampling period. The high-BBA data are shown in red (n=206) and low-BBA data (n=209) in grey. PDFs are expressed as cumulative probability distributions - the contours enclose 25, 50, 75, and 90 % of the data. The light blue shaded region encloses all SCL data, averaged into 30 s bins (n=203). The open triangle, filled circle, solid black curve, and solid grey curve are analogous to those in Fig. 4 and are computed as outlined in Table ~~3.~~2. The blue curve is a mixing curve with moist ~~endmember~~end member centered on the SCL data. Precisions (black bars) and accuracies (red bars) are given near the bottom, where each set of bars corresponds to the small red circle vertically above it.

For the 2018 IOP, the high-BBA air lobe falls along a mixing line with evidence of ET contribution (Fig. ~~10a~~8), but the PDF extends downward and is bound from below by a detrainment curve at 3600 m. The main low-BBA PDF lobe falls near a Rayleigh path, even extending below~~. The majority of this signal is due to air sampled below 3000 m. If these data are removed (Fig. 10b)~~ (the majority of the signal ~~either falls directly along a~~lying below the Rayleigh ~~path, or in a (q, δD) region indicative of convective detrainment as in 2017.~~curve is due to air sampled below 3000 m). An estimation of altitude and temperature were performed using the Rayleigh model separately for

the high vs. low BBA data. Correlations of 0.5 with observed values were found for each group. The low-BBA air has best fit slopes of 0.48 and 0.51 for altitude and temperature. The high-BBA air has best fit slopes of 0.71 and 0.86. δD decreases with altitude by -19 ‰ km^{-1} and -12 ‰ km^{-1} for the low and high BBA groups respectively.

3.43 Evidence of BC scavenging from combined BC/CO and (*q*, *δ*D) measurements

Black carbon can serve as CCN and be permanently removed via precipitation. Carbon monoxide, on the other hand, has a low solubility in water and therefore is not altered significantly by clouds. Consequently, scavenging of BC by precipitation should cause the BC/CO ratio to decrease (e.g. Liu et al., 2020). The FT (*q*, *δ*D) diagrams for the 2017 and 2018 IOPs show that ~~airmasses~~air masses sampled had a variety of integrated precipitation amounts, providing an approach to test for evidence of BC scavenging (2016 was not used because there is minimal occurrence of precipitation). Unlike for the previous section, where distinct ~~airmasses~~air masses were isolated in order to highlight the primary hydrologic processes occurring, all data that likely originate from the African ~~PBL~~planetary boundary layer are used here. The motivation is to diagnose the influence of scavenging on ~~rBC~~BC concentrations for an arbitrary parcel of air. FT data were averaged into 60-s blocks and data with CO less than 100 ppbv were discarded, as they reflect air of marine origin.

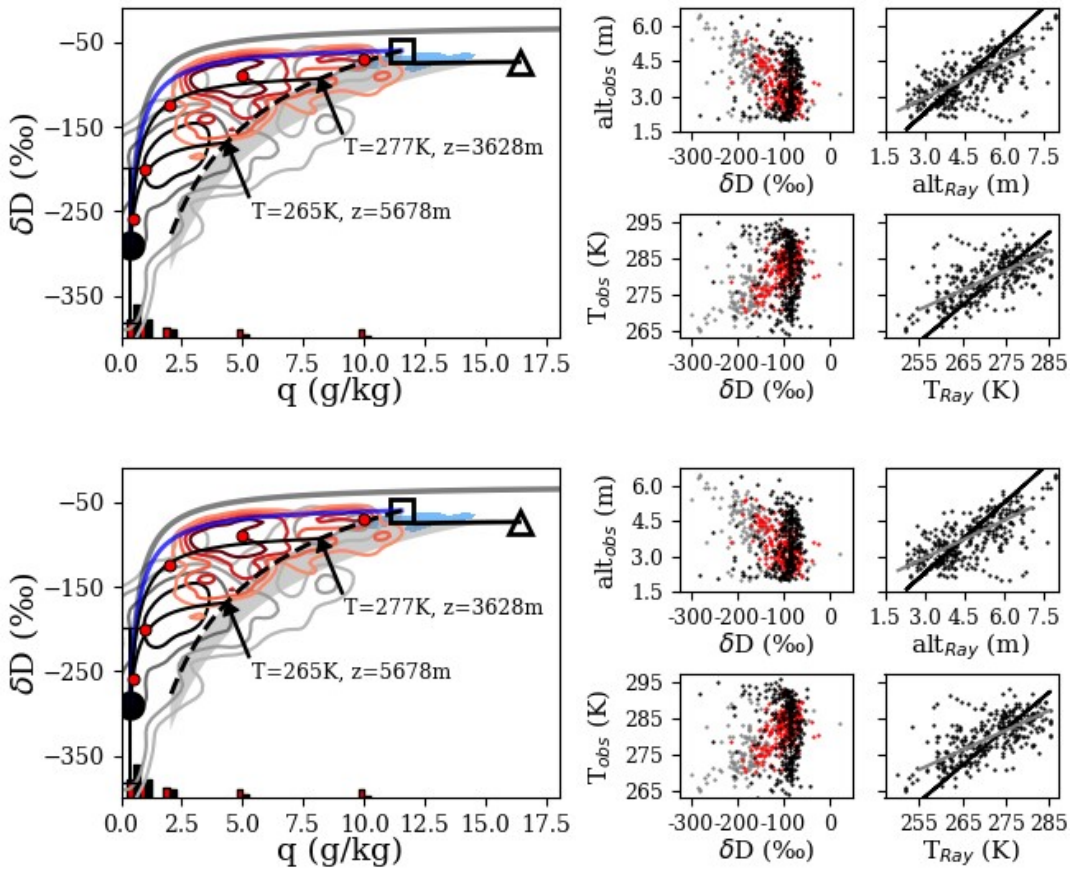

Figure ~~9~~7. (left) Similar to Fig. ~~8~~6 but for the ORACLES 2017 sampling period. Red PDF (n = 218), grey PDF (n = 217), blue shaded region (n = 902), open triangle with black line segment, grey, and blue curves are as in Fig. ~~8~~6. The open square represents mean MBL adjusted for estimated ET contribution as described in Sect. 3.4.3. The blue solid curve is a mixing model. Thin black curves (solid) from the Rayleigh curve (dashed) are detrainment mixing models as described in Section 2.~~6~~5. The light grey shaded region bound Rayleigh processes for all measured SCL initial values. (Center column) *δD* vs height and temperature for 2017 (red, grey) and 2016 (black) data. (Right column) observed heights and temperatures vs. those estimated using the Rayleigh model as detailed in Section 2.~~6~~5, along with best fit (grey) and 1-1 (black) lines.

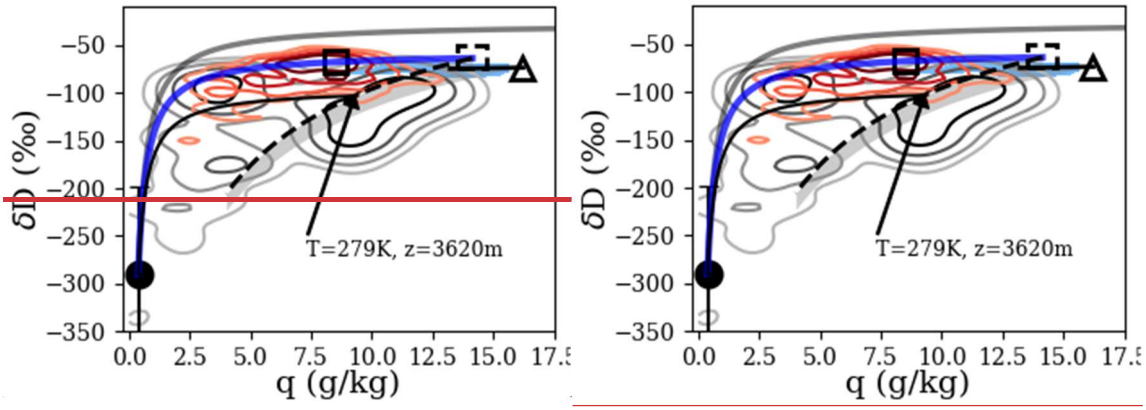

Figure ~~10~~8. Similar to Fig. ~~9~~7 but for the ORACLES 2018 sampling period. All symbols and curves are analogous to those in Fig. ~~9~~7. n = 200, 200, and 780 for the red PDF, grey PDF, and blue shaded regions respectively. The open square near the red PDF is the point along the blue curve where *q* is equal to its mean MERRA 10m value over the solid boxed region of Fig. ~~6~~4.

Figure ~~11~~9 shows clear gradients in BC/CO coloring for (*q*-, *δ*D) space. If one uses the simple detraining convective plume model (outlined at the end of Section 2.~~6~~5) to interpret the joint (*q*-, *δ*D) data, then the BC/CO decreases with increased precipitation amount, which would be expected for scavenging. Because the detrainment mixing curve has little *δ*D variability for $q > 2$ g kg^{-1}, the boxed regions depicted in Fig. ~~11~~9 correspond roughly to relatively low, moderate, and high precipitation amounts. PDFs of BC/CO for these three regions (Fig. ~~12a~~10a,b) separate with statistical significance (at the α=0.05 using a t-test) for both the 2017 and 2018 IOPs. For the 2017 IOP the PDFs means are 9.1, 5.9, and 3.9 ng kg^{-1} ppbv^{-1}. For 2018, the means are 5.1, 3.4, and 1.5 ng^{-1} kg^{-1} ppbv. As a control, the data separated by relatively low, moderate and high values of *q* (bounds of (2,5), (5,8), and (8,11) g kg^{-1} respectively) show no statistically significant separation.

The change in *q* due to precipitation, Δq_{precip}, is computed for each data point in Fig. ~~11~~9 using an approximation to the convective plume model. For $q > 2$ g kg^{-1}, we take the observed *δD* to be equal to that of the plume when it detrained, so that Δq_{precip} can be approximated with the Rayleigh model as.

$$\Delta q_{precip} \sim \left| q_0 - q_{Ray}^{-1}(\delta D_{obs}) \right|, \quad (1)$$

where q_0 is the estimated initial q of the plume before precipitation, q^{-1}_{Ray} ~~is~~ the Rayleigh model inverted to predict q as a function of δD, and δD_{obs} ~~is~~ the observed value. This ~~is~~ difference is intuitively similar to the "rainout fraction", $F = q/q_0$~~),~~) that appears in Rayleigh calculation. The correlation between Δq_{precip} and BC/CO is 0.71 for 2017 and 0.56 for 2018 (Fig. ~~12e~~10c). In comparison, the correlation between q and BC/CO is 0.21 for 2017 and -0.14 for 2018, and distinctly inferior. This result suggests a quantifiable path for deriving BC scavenging coefficients using isotopic data that is unavailable from measures of water concentrations alone.

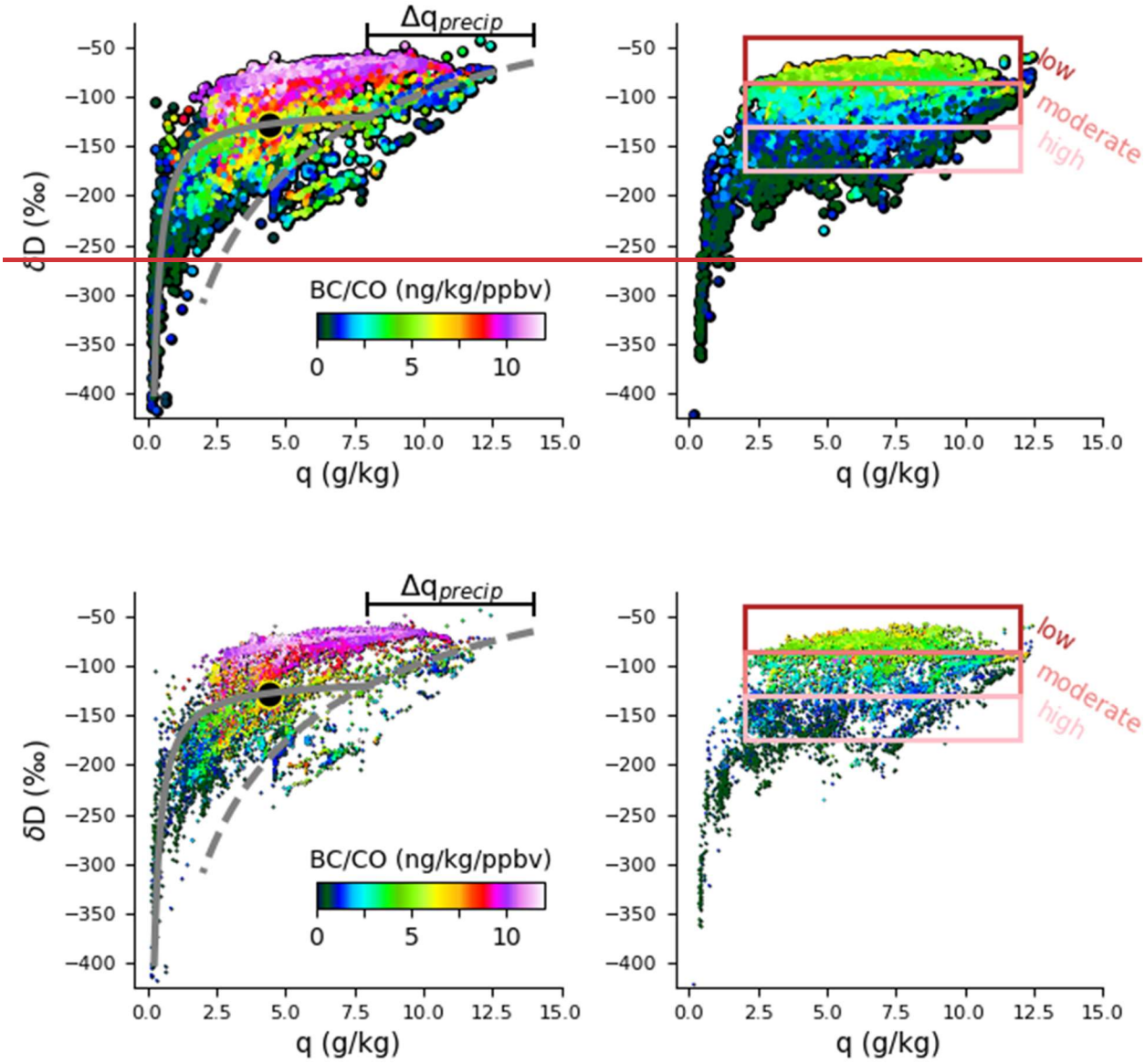

Figure ~~11.~~ 9. (*q*-, δD) diagrams for 2017 (left) and 2018 (right) IOPs, colored by rBC/CO. Grey lines show schematically the regression of the detraining convective plume model onto a sample data point (black filled circle), and the estimated change in *q* due to precipitation. Rectangles (shades of red) show the approximation of this model applied in Figure ~~12~~10 to group a subset of the data into low, moderate and high precipitation amounts.

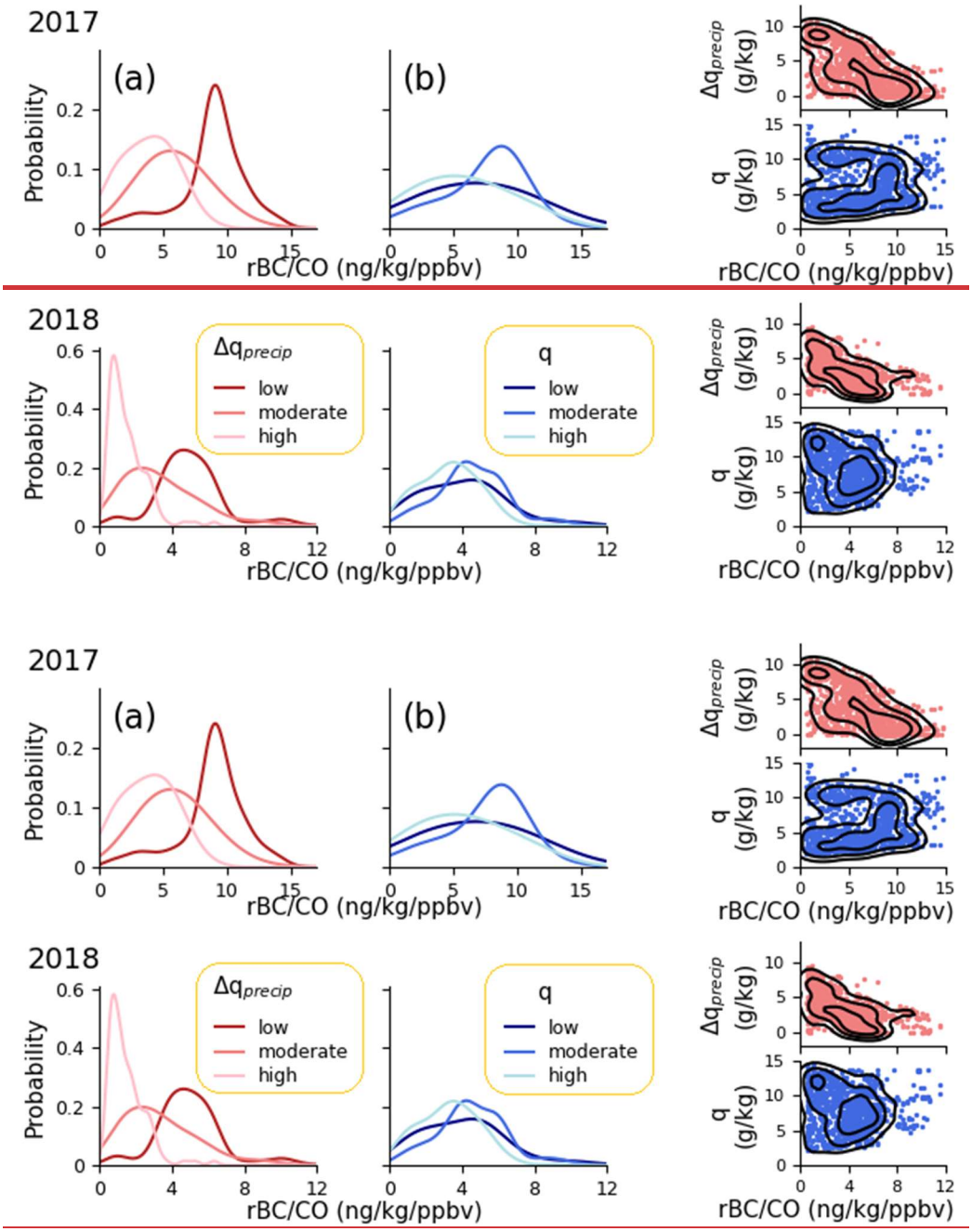

Figure ~~12~~10. Evidence for BC scavenging in FT BBA air using (q, δD) data. (a): rBC/CO PDFs for low, moderate, and high Δq_{precip} as defined in Fig. ~~11~~9, for the 2017 (top row) and 2018 (bottom) IOPs. (b): rBC/CO PDFs for Fig. ~~11~~9 data grouped by low, moderate, and high values of q as detailed in the main text. (c): scatter plots of rBC/CO versus Δq_{precip} and q, with PDF contours overlain.

3.~~5~~4 Entrainment mixing and precipitation in the ~~SCMBL~~stratocumulus-topped MBL

~~Figure 5 shows the range of SCL (q, δD) states captured during ORACLES. This~~The variability of isotopic signals in the MBL is small in comparison to those of the ~~isotopic signal of hydrologic histories of~~ FT ~~air masses, e.g. the δD of the moist endmember is nearly constant given the dynamic range of values higher up. However, it.~~ It was found that for MBLs sampled during ORACLES, the differences between the SCL and CL are small enough to be comparable to or less than SCL variability over the observation period and region. This range makes it more challenging to attribute variations in CL (q, δD) to specific CL processes (e.g. entrainment vs. precipitation) on an absolute scale given the measurement uncertainties. Therefore, CL (q, δD) data are plotted as deviations (Δq, $\Delta\delta$D) from the mean values of the nearby sampled SCL, $(q, \delta D)_{SCL}$, which subtracts out the SCL variations (Fig. ~~13~~11). CL data are taken primarily from LL and SAW modules (processed as in Section 2.4). For these modules, $(q, \delta D)_{SCL}$ were taken from temporally neighboring data below 500 m, which usually occurred within 10 minutes before or after the module, but in some cases ± 20-minute windows were necessary. CL data were taken secondarily from vertical profiles (Section 2.1) which did not include LL or SAW modules. For these profiles, (Δq, $\Delta\delta$D) were computed from the vertically-averaged values of the SCL and CL for the respective profile. Only CL data for which the magnitude of the mean relative wind between the SCL and CL was less than 3.5 m s^{-1} were used to avoid noise due to large relative horizontal advection. Each block of SCL data used for computing $(q, \delta D)_{SCL}$ was also used to compute mean ~~cloud condensation nuclei (~~CCN~~)~~ values. Due to instrument limitations it is necessary to use SCL rather than CL CCN measurements, but Diamond et al (2018) showed that for the 2016 IOP, SCL CCN correlates well with CL droplet number concentration, implying connection between the SCL and CL aerosol concentrations.

Figure ~~13~~11 shows (Δq~~,~~ $\Delta\delta$D) diagrams colored by SCL CCN tercile groups. The CCN terciles are different for each year and are listed in Table 3.~~3.~~ Distributions of SCL CCN are shown in Fig. ~~14~~12. The solid and dashed black curves are mixing and Rayleigh curves. The ~~endmembers~~end members for the mixing curves are $(q, \delta D)_{SCL}$ and the same dry, isotopically depleted ~~endmember~~end member used in figures ~~7-9~~6-8. From here on out this mixing trajectory is referred to as mix_{FT}. Data which fall below mix_{FT} are candidates for precipitation but there are two possibilities. The first is that the CL has a recent history of precipitation. The other is that the air entraining in at CL top tends to align the data along an alternate mixing trajectory. To test this, mixing curves between $(q, \delta D)_{MBL}$ and the mean (q, δD) of the 250 – 500 m region above CL top $(q, \delta D)_{250\text{-}500}$ for all vertical profiles in Sect. 2.3 are included in Fig. ~~13~~11 and from here on out are referred to as $mix_{250\text{-}500}$. They are expressed as (Δq, $\Delta\delta$D) like the scatter points. The dark portion of the curves represent mixtures that have at most 25 % $(q, \delta D)_{250\text{-}500}$ contribution. CLs sampled during the 2016 IOP occurred at higher latitudes in comparison to the other two IOPs and the CLs were on average 2-3x shallower (Fig. ~~14~~12). The majority of CLs show small deviations (Δq < 0.5 g kg^{-1}, $\Delta\delta$D < 4 ‰) from $(q, \delta D)_{SCL}$. The majority of $mix_{250\text{-}500}$ curves (30 out of 35) are centered about mix_{FT} and clearly depart from the Rayleigh trajectory. Five of the curves fall closer to the Rayliegh trajectory.

In comparison to the 2016 IOP, a higher proportion of 2017 IOP data deviate from $(q, \delta D)_{SCL}$, and the standard deviation is larger. There are fewer data points shown for 2017 - since three of the flights were eastward toward Ascension Island, days where the MBL has transitioned to shallow cumulus rather than a ~~SCMBL~~stratocumulus-topped MBL were omitted. Two thirds of the data lie to within precision of one of the mixing curves or the Rayleigh

curve. The other third cannot be described by the simple models presented here. As in the 2016 IOP, the majority of $mix_{250\text{-}500}$ curves are clustered about mix_{FT} (19 of 24) while 5 pass near the Rayleigh trajectory.

For the 2018 IOP, the alternate ~~endmember~~end member mixing curves cover a wide range of (q, δD) space rather than being clustered about $mix_{FT,}$ which likely explains the middle tercile CL data (yellow). Like in the 2017 case, the data which lie near a Rayleigh trajectory with $\Delta\delta D > 5$ ‰ (blue cluster) could not be explained by mixing curves unless the CL contained a fraction of FT air greater than 25 % in comparison to the SCL.

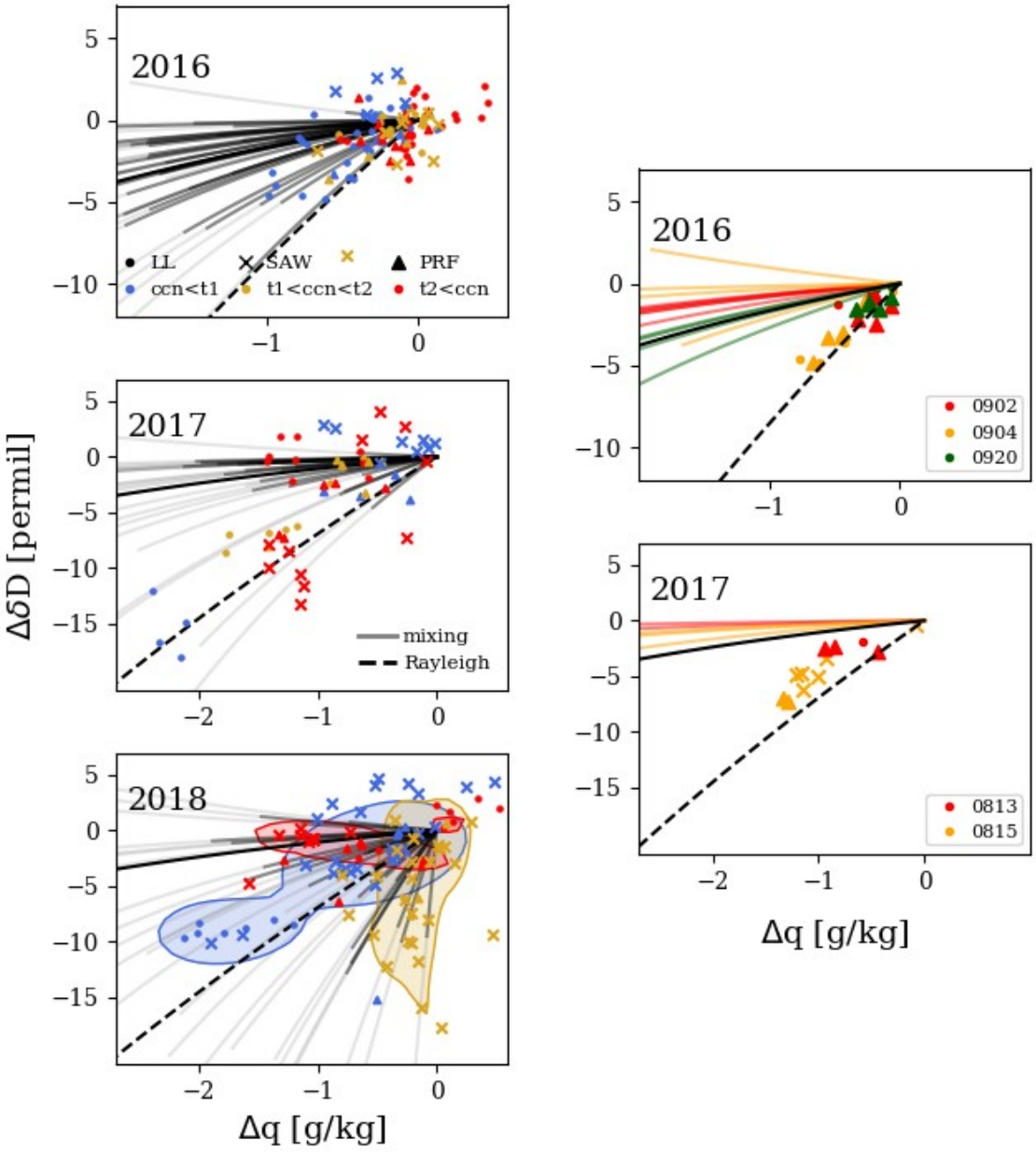
2016
2017
2018
LL
SAW
PRF
ccn<t1
t1<ccn<t2
t2<ccn
mixing
Rayleigh
Δδ D [permil]
Δq [g/kg]
0902
0904
0920
0813
0815

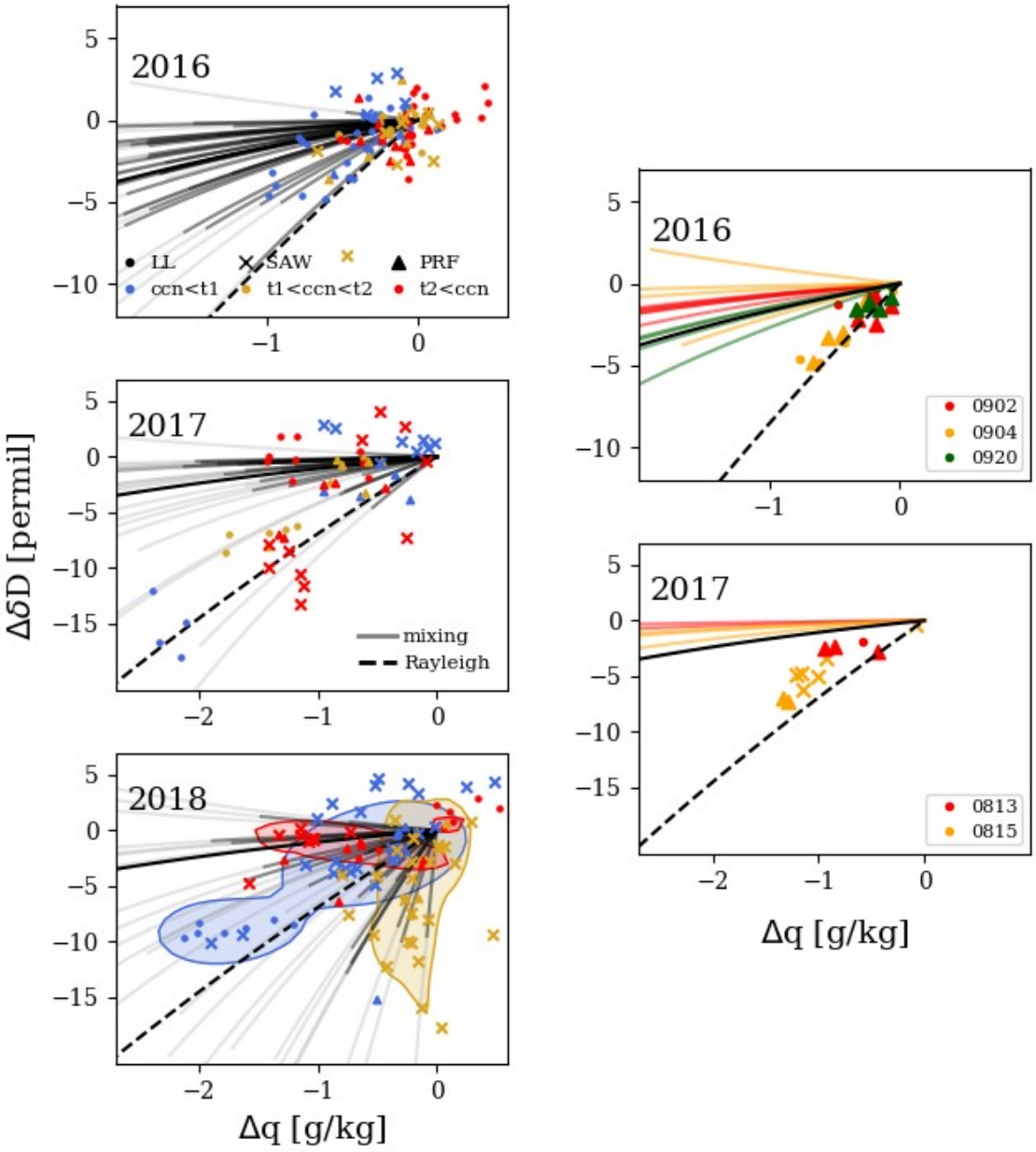

Figure ~~13~~11. (Left column) CL (*q, δD*) data expressed as deviations from the nearby SCL mean values, as described in the main text. Symbols denote the flight module types level leg (LL), sawtooth pattern (SAW) and vertical profiles (PRF). Colors denote tercile groups for SCL CCN (terciles listed in Table 3.3). (Right column) Data from several flights during the 2016 and 2017 IOPs are isolated. These data fall near a Rayleigh trajectory and cannot be explained by mixing with the overlying FT measurements for that day.

Table 3. Sub-cloud CCN (cm^{-3}) terciles for the groupings in Fig. ~~13~~11.

IOP year	min	tercile 1	tercile 2	max
2016	19	134	221	426
2017	41	186	357	926
2018	16	188	250	460

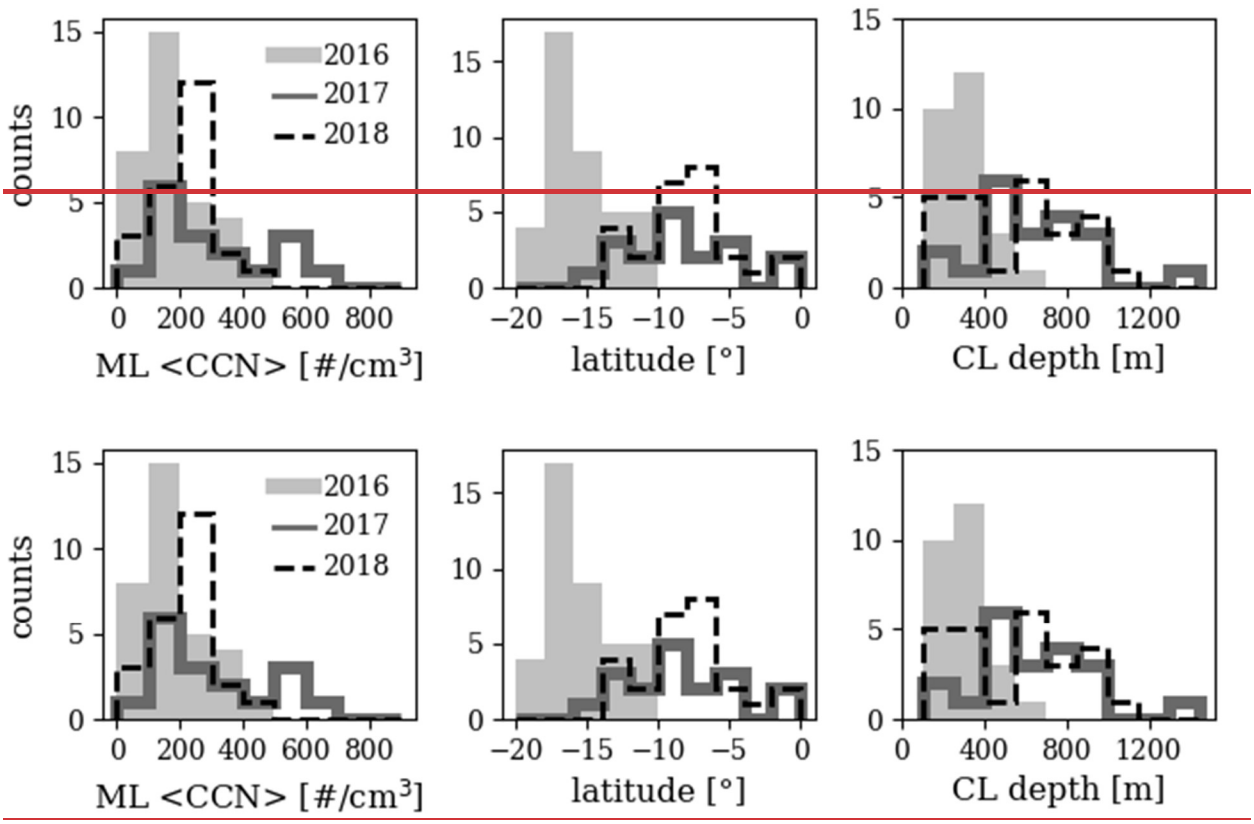

Figure ~~14~~12. Histograms of SCL CCN (left), CL sampling latitudes (middle), and CL depths (right) for each IOP.

~~5~~4 Discussion

~~*Sub-cloud layer δD*~~

~~In this study the sub-cloud layer *δD* has been assessed, briefly, for agreement with basic theory as well as typical variations. Agreement with theory has been assessed on two different scales: the coarser scale of Figure 8-10 and the finer scale of Figure 5. For the former, it was confirmed that to first order, median values for each IOP lie within~~

~~7 ‰ to mixing curves between vapor at equilibrium with a mean SST and dry FT air, giving the expected result that the primary moisture source for the SCL is ocean evaporation as opposed to evapotranspiration from a land source. However, to advance theory of oceanic isotopic exchange observational constraints better than 7 ‰ are needed (e.g. Benetti et al., 2018; Feng et al., 2019). A more detailed comparison of the data with an MJ79 prediction shows disagreements of 10 ‰ for individual data points. A large source of variation for the predictions is the assumed δD of the ocean for which there are no measurements during ORACLES. Using Fig. 4 of Benetti et al. (2017) as a guide, an ocean surface δD_{oc} of 0 – 6 ‰ is reasonable for the 2017 and 2018 IOPs. The MJ79 predictions using 6 ‰ provide a rough upper bound on the SCL measurements for 2017 and 2018 (Fig. 5), which makes sense since FT entrainment and precipitation could decrease SCL δD. For 2016, even a δD_{oc} of 10 ‰ does not provide an adequate upper bound. One possibility is that δD_{oc} is even higher than estimated. Another is the WISPER system calibration uncertainty to the absolute scale, which is comparable to the difference from this campaign (see Henze et al., 2022).~~

~~Additionally, variability throughout the SCL column has been assessed, which is novel since data above the surface (e.g. sampling from ship masts ~30 m) are uncommon. The SCL is characterized in part by nearly constant vertical profiles of quantities such as water concentration and potential temperature, and similarly the isotope ratios are expected to as well. The right column of Fig. 5 shows that this is often the case for δD. Vertical deviations over the layers are small, typically less than 2 ‰. These deviations are smallest for 2016, which is reasonable given the shallower SCMBLs would likely be more coupled to the surface. Additionally, the speed of the aircraft affords a snapshot of an SCL's horizontal variability, as opposed to surface (ship or island) based measurements which must rely on advection. Horizontal P-3 legs show that even over distances of 50 km (6 minutes of P-3 travel time), 10 s averages of δD typically do not vary by more than 2 ‰.~~

FT and BBA plume hydrologic histories

Figures ~~6~~4 and ~~7~~5 show that FT air from the 2016 sampling period experienced the least amount of precipitation while over Africa of the three sampling periods. The in-situ (q, δD) data show that in fact there is almost no signs of precipitation in the sampled high-BBA air in 2016. ~~The center of the high-BBA PDF falls almost directly on a mixing curve between the center of the SCL observations and dry FT air, and the orientation of the PDF follows the mixing trajectory well.~~ The PDF is enveloped from above by the theoretical ET mixing curve, suggesting ET contributions for some of the measurements, although the dominant signal is simple mixing with air close to the observed SCL values. This is interpreted as evidence of minimal ET contribution to the African planetary boundary layer air, and therefore its moisture content closely resembles the original marine source which advected onto the continent. The low-BBA data are shown for completeness, but since back-trajectories suggest they often originate from the southern Atlantic rather than Africa, they are not analyzed in detail.

Both high-BBA and low-BBA data for the 2017 IOP show signs of precipitation (Fig. ~~9~~7). The data are bound from above by a mixing curve with a moist end member including 25% ET contribution and from the right by a family of Rayleigh curves. The data support a depiction of the air mass hydrologic history as convective detrainment followed by dilution; ~~airmasses~~air masses follow the Rayleigh curve during moist convection (i.e., condensation with high

precipitation efficiency), then begin to detrain remaining total water at their level of neutral buoyancy, and subsequently form a diluted mixture with surrounding dry FT air. The low-BBA air is associated with convection which reached higher altitudes. A correlation of -0.67 for δD vs. height is obtained, whereas the correlation is close to 0 for the 2016 IOP despite sampling at a similar altitude range. For the 2017 IOP, detrainment heights and temperatures predicted from the Rayleigh model both have correlations of 0.67 with the observations, which is remarkable considering the simplicity of the parcel-type model used to describe the entire study period~~:~~. That is, a single choice of values for surface T, q, and height, no entrainment during convection, and all condensate converted to precipitation provides a reasonable first approximation. The best fit lines have slopes of 0.54, however. Possible reasons why this slope is less than 1 include variation in surface conditions during convection throughout the observation period, and precipitation efficiency less than unity. With respect to that latter, entrainment into an updraft would decrease δD more than expected from the Rayleigh process alone. Therefore, to achieve the same δD with only a Rayleigh process, the parcel would have to be lifted higher to compensate. Additionally, δD along detrainment curves was taken as constant to simplify the calculations. However, δD decreases by about 20 ‰ once detrained updraft air has been diluted to around 2 g kg^{-1}, resulting in the same bias for the Rayleigh model as precipitation efficiency < 1 does.

The Oct. 2018 sampling period comprises elements of both the 2016 and 2017 sampling periods. The high-BBA comes from higher latitudes similar to 2016, while the low-BBA air is further north with more rainfall. However, unlike 2016, the high BBA air flows northwest over Africa before flowing offshore. The high-BBA air (q, δD) signal reflects this, the PDF lobe falls along a mixing line with evidence of up to 25 % ET contribution, but the distribution extends below the mixing line much more so than in 2016, bounded beneath by detrainment at 3600 m. Meanwhile, a large fraction of the low-BBA data lies near or below a Rayleigh curve, suggesting convection with a high precipitation efficiency and little subsequent mixing and potentially re-evaporation of falling droplets. Data with this signal are almost exclusively at heights below 3000 m, while data above 3000 m either fall directly on a Rayleigh curve or in the region hypothesized to be detrainment. Perhaps rain droplets falling from these higher altitudes are partially evaporating into the air below 3000 m. Such refined hydrologic history is not readily extracted without more detailed modeling.

Parsing entrainment mixing vs. precipitation in the CL and detection timescales

Cloud layer data for the 2017 and 2018 IOPs deviate further from their respective $(q, \delta D)_{SCL}$ values in comparison to the 2016 IOP. This is in line with the deeper CLs (Fig. ~~14~~12) transitioning to cumulus coupled CLs, becoming less well-mixed with the SCL, and experiencing higher entrainment and precipitation rates. CL (q, δD) measurements for all IOPs are poorly constrained by the simple mix_{FT} and Rayleigh models – around 50 % of data for the 2016 and 2017 IOPs lie within these models, and only 30 % for the 2018 IOP. For the 2018 IOP, the majority of data outside these bounds can be explained by mixing with air masses above the MBL which have varying (q, δD) values. For the 2016 and 2017 IOPs, even alternate ~~endmember~~end member mixing cannot explain the data and these exceptions merit further study since the fraction of the data they make up is non-negligible. One possibility is the choice of a

single representative (q, δD) pair for the SCL when generating the $mix_{250\text{-}500}$ curves. If either or both of q and δD for overlying air were higher than the SCL values, the resulting mixing curves could explain the data in question. Differential horizontal advection of the MBL and FT could also be a contributing factor.

Although the data show signals of local precipitation in the 2016 and 2017 IOPs, the null hypothesis that all data falling below the mix_{FT} curve came from $mix_{250\text{-}500}$ curves cannot be fully ruled out with this analysis alone. However, Fig. ~~13~~11 (right column) highlights some cases where the data fall near a Rayleigh trajectory and cannot be accounted for by mixing models with overlying FT air sampled on those days. Previous work has highlighted the uncertainties involved with assuming an MBL is in significant contact with the FT air above it at the time of sampling and neglecting horizontal advection (Diamond et al., 2018). Therefore, it cannot be definitively concluded that the cloud layers sampled during the highlighted flights recently precipitated. However, these flights would be good candidates to examine with advanced modeling.

Assuming that at least some of the signal is due to precipitation, the question arises regarding the time period prior to the measurement during which the precipitation occurred. Simple bulk model studies (Schubert et al., 1979; Bretherton et al., 2010; Jones et al., 2014) estimate a thermodynamic re-equilibration time scale of a ~~SCMBL~~stratocumulus-topped MBL at 0.5 - 1 day. Therefore, at longer timescales it is assumed that any isotopic evidence due to precipitation has been 'erased' by subsequent turbulent mixing, including influences from surface evaporation, and consequently any signals detected are from precipitation that occurred within the past day. Previous observational studies show ~~SCMBLs~~stratocumulus-topped MBLs precipitate primarily at night or the early morning hours (Burleyson et al., 2013, Leon et al~~.~~., 2008, Comstock et al~~.~~., 2004). ~~This argument is consistent either the weaker signals observed in the SCMBLD in the ORACLES dataset.~~ It may be the case that the majority of precipitation signals detected with isotope measurements are from the morning on the same day as sampling.

(q, δD) signals and SCL CCN

By inspection, there is weak SCL CCN clustering in Fig. ~~13~~11 for the 2016 IOP. The two higher CCN tercile groups cluster about the origin while the lowest CCN tercile group extends to more negative values. If only a fraction of the signals come from $mix_{25\text{-}500}$ processes, the data would indicate that aerosol loading has induced precipitation suppression. The converse could also be the case: aerosol scavenging in ~~SCMBLs~~MBLs with previous precipitation ~~result~~results in lower SCL CCN. Microphysical modeling would be required to quantify the causality. Further, no clear clustering is present for the 2017 IOP, in part due to the smaller signals. Indeed, using either thermodynamic or isotopic measurements to assess cloud aerosol interactions in ~~SCMBL~~the MBL is not necessarily achievable with simple analytical models. As a case in point, one confounding factor could be locally enhanced entrainment due to precipitation (see e.g. Fig. ~~11~~9 in Wood, 2012), which could replenish BBA aerosols which were scavenged.

For the 2018 IOP, a consistent explanation develops from Fig. ~~10~~8 and Fig. ~~13~~11 (which present the 2018 IOP FT and CL data respectively). CL data in the middle and top SCL CCN tercile groups are largely clustered around mix_{FT} or the region below the Rayleigh curve (Fig. ~~13~~11, shaded regions). Of these data, the highest tercile group is

primarily along the former while the middle group is along the latter. This is consistent with the (q, δD) location of high vs. low BBA FT PDFs in Fig. ~~10~~8, if they were to serve as the above MBL mixing ~~endmembers~~end members. Therefore, the CL data in the middle and top tercile groups are likely both mixtures of SCL and FT air, with the differences in MBL CCN due to the differences in FT BBA levels. Data in the lowest tercile cluster closer to a Rayleigh trajectory, possibly indicating local precipitation and aerosol scavenging. This self-consistency in the joint (q-, δD) measurements builds a degree of confidence that CL isotopic signals can be connected to entrainment processes, and potentially precipitation, even if the connection is more detailed as for the 2017 IOP.

~~6~~5 Final Remarks

~~The~~ This study utilizes in-situ measurements taken during ORACLES ~~FT~~over three IOPs across three years in the southern hemisphere late winter period (August-October), with 39 flights and in total ~312 hours of measurements. The FT air mass histories are deduced using the process-based expectation of variations in (q, δD) space, described by simple analytical models, in combination ~~of~~with several other data sources (satellite, reanalysis, and GCM output). The graphical framework is convenient to develop qualitative (and potentially quantitative) estimates of moisture contributions from different processes along the atmospheric transport pathways of water vapor (e.g. fraction of moisture from ET and convective detrainment heights). The analysis partitions ~~airmasses~~air masses into those which enter the FT via dry convection/vertical-mixing vs. via convection accompanied by cloud formation and precipitation. In 2016 the BBA air entered into the FT almost entirely by vertical mixing: likely exported latterly from the continental ~~PBL~~planetary boundary layer, with dilution of FT air aloft. In contrast, in 2017 both high and low BBA FT air are primarily associated with convective detrainment, where measurements provide evidence that low-BBA air is associated with ~~-~~convective detrainment at higher altitudes. In 2018, the lower BBA air experienced precipitation. In fact, most measurements indicate that direct convection (e.g., minimal dilution after detrainment) was sampled, and considerable fractions of low-BBA air lying below the Rayleigh curve is indicative of partial re-evaporation of falling rain drops. High-BBA air for 2018 shows a combination of mixing with ET contribution and convective detrainment which is important to the hydrologic picture.

There is strong correlation between (q, δD) evidence of precipitation and BC/CO evidence of scavenging~~.~~ in FT BBA plumes. As a control, BC/CO along mixing trajectories show little consistency. Change in q due to precipitation, Δq_{precip}, derived from the isotopic data is correlated with BC/CO, 0.71 for 2017 and 0.56 for 2018. This diagnostic partitioning cannot be achieved with the humidity measurements alone - correlation between q and BC/CO is 0.21 for 2017 and -0.14 for 2018. Some previous studies on black carbon scavenging use BC properties and BC/CO ratios in cloud droplets (Ohata et al., 2016; Liu et al., 2020; Twohy et al., 2021) to assess scavenging

mechanisms and coefficients. However, they are unable to link their results to the integrated precipitation amount. Here, because the isotopic data serve as an independent measure of integrated precipitation (rather than a precipitation rate as with radar), they may provide a unique and ~~complimentary~~complementary way of determining BC scavenging in the FT. For the analysis presented here, BC concentrations in the African ~~PBL~~planetary boundary layer would be required to derive numerical values for the scavenging coefficient. An ideal sampling strategy would observe the (*q, δ*D~~,~~), and BC of air within and above the ~~PBL~~planetary boundary layer simultaneously measured in a Lagrangian framework, providing direct values of Δq_{precip}, the change in BC, and in turn a scavenging coefficient.

Next, a test of whether a (*q, δ*D) analysis could detect recently precipitating stratocumulus MBLs was performed. An analysis utilizing relative differences between the SCL and CL was chosen due to large measurement uncertainties and lack of ocean surface *δ*D measurements. This posed challenges since relative differences in *δ*D between these two vertical regions tend to be small. While no strong statements on precipitation or their interaction with aerosols can be made from this study, several key conclusions are made. For all IOPs, the fact that the CL is coupled to the surface will tend to erase signals of precipitation events, or at least convolute them with other ~~process~~processes. From previous studies, it is inferred that the time scale at which this occurs to be 0.5 - 1 day. However, by far the most difficult obstacle for the ORACLES dataset is the ambiguity in CL signals due to variability in (*q, δ*D) of the entraining air. Some air masses sampled above cloud top had values that, if entrained into the CL, were capable of lowering the CL *δ*D values towards a region of (*q, δ*D) space that would otherwise appear as precipitation. Such ~~airmasses~~air masses were observed about 14%, 20 %, and 60 % of the time for the 2016, 2017, and 2018 IOPs respectively. For the 2016 IOP, the data which do suggest recent precipitation are typically connected to MBLs with the lowest SCL CCN values, which could reflect aerosol scavenging. For 2018 IOP, the CL (*q, δ*D) data is combined with SCL CCN values and the FT (*q, δ*D) diagram to ~~summarize~~develop a hypothesis for the regional conditions: the middle and highest CCN values in the MBL are likely connected with variation in aerosol levels of entraining air, while the lowest MBL CCN values are the result of local precipitation. It may be the case that simply looking at relative differences between the SCL and CL does not produce an adequate signal, but that an MBL which experiences precipitation, even with subsequent mixing, can produce a column-averaged *δD* lower than that for an MBL with only mixing and no precipitation. More complex models appear necessary to obtain constraints on precipitation versus entrainment mixing and their effects on MBL aerosol concentration. Nonetheless, this study provides evidence that such models could potentially produce these constraints, when coupled with targeted observations, and are worth pursuing further.

Appendix A: Estimating evapotranspiration contribution to total water mass of a boundary layer column

Because ET contribution can alter the isotopic content of an ~~airmass~~air mass, its expected fraction of moisture contribution for each sampling period was estimated using the following back of the ~~envelop~~envelope calculation. For a marine boundary layer column with cross-sectional area ~~1m^2~~1 m^2, the total mass of water in the column $m_{H2O,col} \sim hq_a\rho_a$, where h is the height of the column, and q_a, ρ_a are the column-average specific humidity and air

density. If the column advects onto land, then the total mass of water added to the column by ET over some time Δt is $m_{H2O,ET} = (ET)\Delta t$, where ET is the mean net evapotranspiration in units of kg m^{-2} s^{-1}. Therefore, assuming negligible input of water from free tropospheric entrainment, the fraction of ET contribution is $m_{H2O,ET}/(m_{H2O,ET} + m_{H2O,col})$. ET is estimated using the MODIS/TERRA Version 6 Evapotranspiration/Latent Heat Flux product (MOD16A2), taking the mean and standard deviation over the boxed regions of Fig. 5.

Appendix B: Identifying distinct FT air masses

For the FT analysis, it was desired to highlight hydrologic histories of distinct air masses from the African continent (e.g. different BBA plumes), rather than any subsequent mixing between them as they advect westward to the southeast Atlantic. Therefore, distinct FT air masses in each vertical profile were identified using a pseudo-conservative variable approach to highlight the differing hydrologic histories rather than the subsequent mixtures between them. Simple two end member mixing processes are found as straight lines on the diagram while curved segments signal non-conservative processes such as precipitation, or more complex mixing environments (such as multiple sources or time evolving end members). Diagrams of q vs equivalent potential temperature (θ_e) have been used before to identify regions of mixing in atmospheric profiles as well as the mixing end members (Paluch, 1979; Betts and Albrecht, 1987). Here, instead of θ_e, the quantity $q\delta D = q_{HDO}/R_{D,SMOW} - q$ is utilized (since the mixing ratios q_{HDO} and q are both conserved in mixing processes, so is the linear combination $q\delta D$).

P-3 vertical profiles as identified in Section 2.3 were averaged into 25m altitude bins and their trajectories in q vs $q\delta D$ space were visually broken into piecewise segments. Figure B.1 shows an example of segment identification, with associated profiles of thermodynamic quantities and the BBA indicator rBC. The diagram of q vs $q\delta D$ shows a series of piecewise segments, where the corners/kinks are taken as the independent end members (open circles). The vertical profiles show that these air masses correspond to minima/maxima in the profiles of (q, δD), and rBC, or are near kinks in the θ profile, supporting the validity of this method. Although some of these air masses reside in the MBL, only the FT air masses were used.

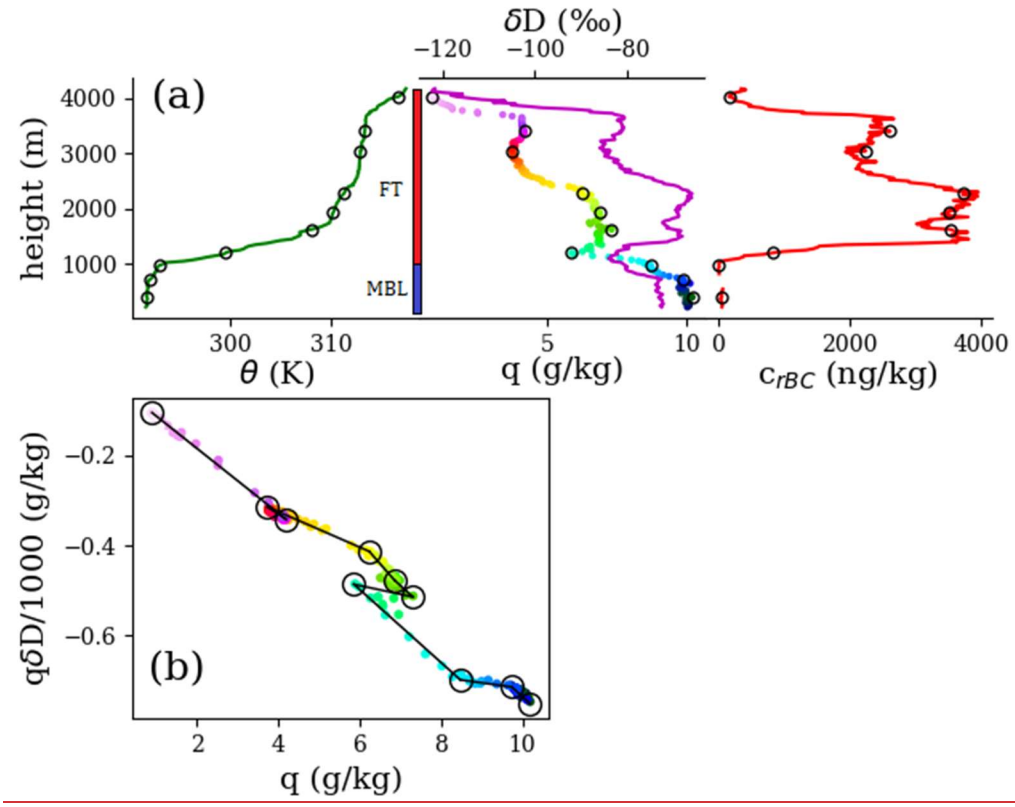

Figure B.1. (a) One of the P-3 vertical profiles on the Sept. 4, 2016 flight, averaged into 25m bins. Profiles of in-situ potential temperature (green), total water mixing ratio colored by altitude, δD (magenta), and refractory black carbon (red). (b) q vs. qδD for the profile, with the same altitude-coloring as the total water profile. Open circles in (a) and (b) mark distinct air masses as outlined in Sect. 3.3.5, identified visually from (b).

Appendix C: Sub-cloud layer (q, δD) and their variances

Figure C.1 shows SCL data averaged into 60 s blocks, where the SCL was identified as in Sect. 3.3.3. Data below 150 m are colored by SST. SST was determined by collocating NOAA COBE monthly mean SST satellite data with the position of the aircraft. Previous studies have been devoted to a detailed understanding of the isotopic composition of the SCL, typically using either land or ship-based measurements (e.g. Benetti et al., 2018; Feng et al., 2019). Rather than testing those analyses in detail, the ORACLES SCL data are shown here briefly for context as a basis for the novel aspects of the aircraft profile dataset. Nonetheless, Figure C.1 includes δD predictions using the simple model of Merlivat and Jouzel, 1979 (MJ79). The MJ79 model – which assumes SCL moisture comes solely from ocean evaporation - was not originally intended for regional scale and sub-daily predictions and its limitations in doing so have been investigated elsewhere (e.g. Jouzel and Koster, 1996; Kurita, 2013). The MJ79 model reduces SCL δD to a simple function of SST and relative humidity with respect to SST (RHS), and provides a useful reference point. For each 60 s average, the MJ79 formula was used for ocean δD values in the range of 0 ‰ to 6 ‰ for the 2017 and 2018 IOPs, and in the range 0 ‰ to 10 ‰ for 2016. The range was used to account for uncertainty

in the ocean isotopic values which were not sampled during ORACLES. The upper bounds were taken by inspection of Fig. 4 in Benetti et al., (2017).

The right column of Fig. C.1 provides a metric of variability in the SCL. The histograms show the difference between means of the lower and upper most sampled 100 m of the SCL for each vertical profile in Section 2.3. The standard vertical difference is about 1 ‰ for 2016 and 2 ‰ for the other two IOPs. Horizontal variability is also explored. Horizontal aircraft legs below 500 m and lasting at least 3 minutes were averaged into 10 s blocks and then the standard deviation of the entire leg was computed. The median horizontal standard deviations are roughly the same as the standard vertical variabilities for 2016 and 2017. For 2018, the median horizontal variability is 1.25 ‰, slightly less than the 2 ‰ vertical variability.

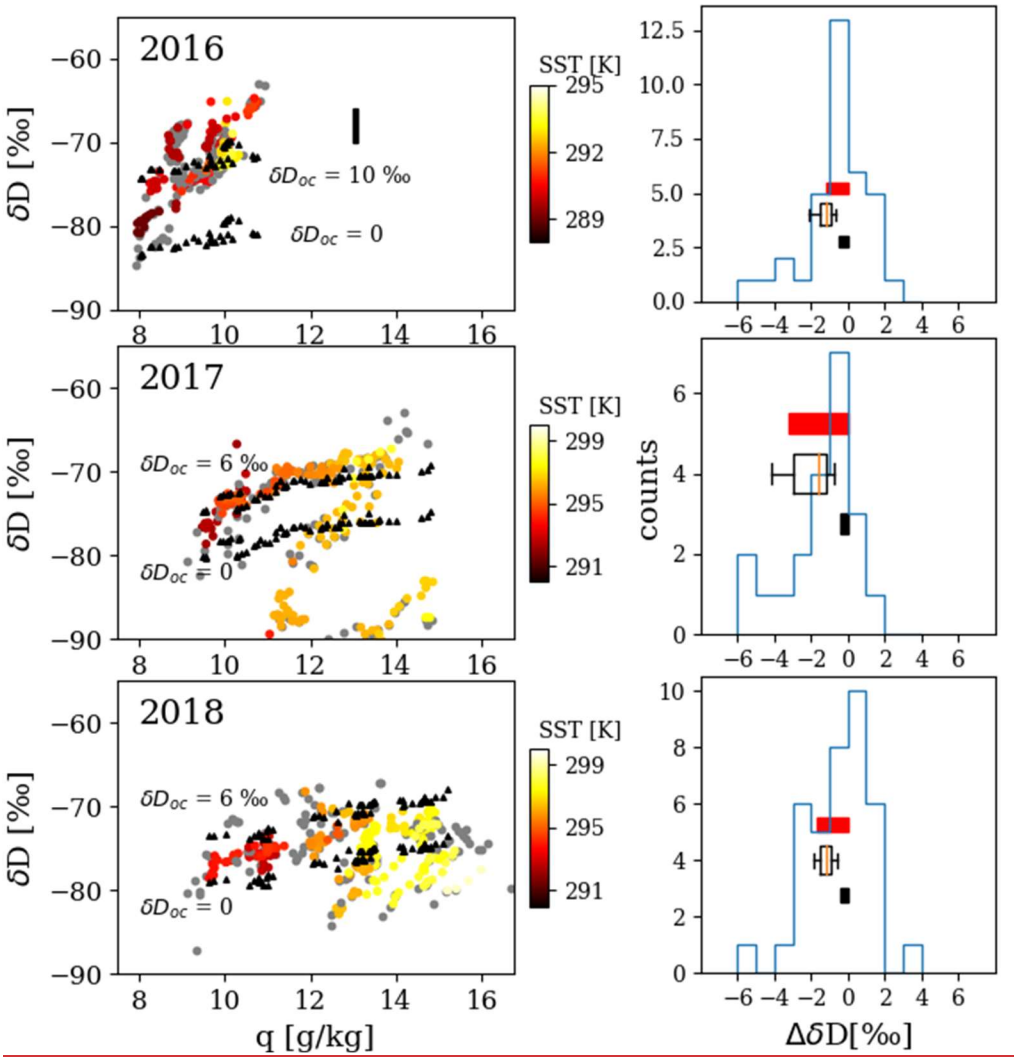

Figure C.1. (Left column) (*q*, *δD*) data in the SCL for 2016 (top), 2017 (middle), and 2018 (bottom), averaged into 60 s blocks. Measurements below 150 m height are colored by NOAA COBE monthly mean satellite SST. Black triangles show predictions using the Merlivat and Jouzel (1979) closure assumption. The vertical black bar displayed for 2016 is the instrument standard error on an absolute scale. (Right column) Histograms of the difference in *δD* between the top and bottom most sampled 100 m of the SCL for each vertical profile. Red bars are the standard deviations of the histograms.

Box plots are the *δD* standard deviations of all P-3 horizontal legs below 500 m height and lasting at least 3 min averaged to 0.1 Hz (n = 23, 22, 25 for 2016, 17, 18 IOPs). Black bars are 0.1 Hz instrument precisions. All standard deviations are multiplied by -1 for visuals.

Author Contributions

DH carried out the formal analysis and visualization, and prepared the manuscript with contributions from all co-authors. DN obtained funding for the project, contributed to analysis conceptualization, and provided supervision. DT provided resources and critical guidance to place the analysis in the context of aerosol and black carbon research.

Competing Interests

The authors declare that they have no conflict of interest.

References

Ackerman, A. S., Toon, O. B., Stevens, D. E., Heymsfield, A. J., Ramanathan, V., and Welton, E. J.: Reduction of tropical cloudiness by soot, Science, 288, 1042-1047, doi:10.1126/science.288.5468.1042, 2000.

Adebiyi, A., and Zuidema, P.: The Role of the Southern African Easterly Jet in Modifying the Southeast Atlantic Aerosol and Cloud Environments, Q. J. Roy. Meteor. Soc., 142, 697, 1574–89. doi:10.1002/qj.2765, 2016.

Albrecht, B. A.: Aerosols, cloud microphysics, and fractional cloudiness. Science, 245(4923), 1227-1230, doi:~~10.1126/science.245.4923.1227,~~ 10.1126/science.245.4923.1227, 1989.

Bailey, A., Toohey, D., and Noone, D.: Characterizing moisture exchange between the Hawaiian convective boundary layer and free troposphere using stable isotopes in water. J. Geophys. Res. Atmos., 118, 8208.8221, doi:10.1002/jgrd.50639, 2013.

Benetti, M., Aloisi, G., Reverdin, G., Risi, C., and Seze, G.: Importance of boundary layer mixing for the isotopic composition of surface vapor over the subtropical North Atlantic Ocean, J. Geophys. Res. Atmos., 120, 2190–2209, doi:10.1002/2014JD021947, 2015.

Benetti, M., Reverdin, G., Aloisi, G., and Sveinbjörnsdóttir, A.: Stable isotopes in surface waters of the Atlantic Ocean: Indicators of ocean-atmosphere water fluxes and oceanic mixing processes, J. Geophys. Res. Oceans, 122, 4723–4742, doi:10.1002/2017JC012712, 2017.

Benetti, M., Lacour, J.-L., Sveinbjörnsdóttir, A. E., Aloisi, G., Reverdin, G., Risi, C., ~~Peters~~Peters, A. J., ~~Steen-Larsen, H.~~Steen-Larsen, H. C.: A framework to study mixing processes in the marine boundary layer using water vapor isotope measurements. Geophys. Res. Lett., 45, 2524–2532. ~~doi:10.1002/2018GL077167~~doi:10.1002/2018GL077167, 2018.

Betts, A. K. and Albrecht, B. A.: Conserved Variable Analysis of the Convective Boundary Layer Thermodynamic Structure over the Tropical Oceans, Journal of Atmospheric Sciences, 44(1), 83-99, ~~doi:10.1175/1520-~~

0469(1987)044<0083:CVAOTC>2.0.CO;2, 1987.doi:10.1175/1520-0469(1987)044<0083:CVAOTC>2.0.CO;2, 1987.

Bond, T. C., Doherty, S. J., Fahey, D. W., Forster, P. M., Berntsen, T., DeAngelo, B. J., Flanner, M. G., Ghan, S., Kärcher, B., Koch, D., Kinne, S., Kondo, Y., Quinn, P. K., Sarofim, M. C., Schultz, M. G., Schulz, M., Venkataraman, C., Zhang, H., Zhang, S., Bellouin, N., Guttikunda, S. K., Hopke, P. K., Jacobson, M. Z., Kaiser, J. W., Klimont, Z., Lohmann, U., Schwarz, J. P., Shindell, D., Storelvmo, T., Warren, S. G., Zender, C. S.: Bounding the role of black carbon in the climate system: A scientific assessment, J. Geophys. Res. Atmos., 118, 5380–5552, doi:10.1002/jgrd.50171, 2013.

Bretherton, C. S., Uchida, J., and Blossey, P. N.: Slow Manifolds and Multiple Equilibria in Stratocumulus-Capped Boundary Layers, J. Adv. Model. Earth Syst., 2, 14, doi:10.3894/JAMES.2010.2.1410.3894/JAMES.2010.2.14, 2010.

Burleyson, C. D., de Szoeke, S. P., Yuter, S. E., Wilbanks, M., & Brewer, W. A.: Ship-Based Observations of the Diurnal Cycle of Southeast Pacific Marine Stratocumulus Clouds and Precipitation, J. Atmos. Sci., 70(12), 3876-3894, doi:10.1175/JAS-D-13-01.1, 2013.doi:10.1175/JAS-D-13-01.1, 2013.

Chand, D., Wood, R., T. Anderson, Satheesh, S. K., and Charlson, R. J.: Satellite-derived direct radiative effect of aerosols dependent on cloud cover. Nature Geoscience, 2, 181-184, doi:10.1038/ngeo437, 2009.

Comstock, K.K., Wood, R., Yuter, S.E., & Bretherton, C.S.: Reflectivity and rain rate in and below drizzling stratocumulus. Quarterly Journal of the Royal Meteorological Society, 130, doi:10.1256/QJ.03.18710.1256/QJ.03.187, 2004.

Diamond, M. S., Dobracki, A., Freitag, S., Small Griswold, J. D., Heikkila, A., Howell, S. G., Kacarab, M. E., Podolske, J. R., Saide, P. E., Wood, R.: Time-dependent entrainment of smoke presents an observational challenge for assessing aerosol–cloud interactions over the southeast Atlantic Ocean, Atmos. Chem. Phys., 18, 14623–14636, 2018, doi:10.5194/acp-18-14623-2018doi:10.5194/acp-18-14623-2018, 2018.

Draxler, R.R.: HYSPLIT_4 User's Guide, NOAA Technical Memorandum ERL ARL-230, 1999 (Latest revision February 2018).

Draxler, R.R., and Hess, G.D.: Description of the Hysplit_4 modeling system, NOAA Technical Memorandum ERL ARL-224, 1997.

Dusek, U., Reischl, G. P., and Hitzenberger, R.: CCN activation of pure and coated carbon black particles, Environ. Sci. Technol., 40(4), 1223–1230, doi:10.1021/es0503478, 2006.

Feng, X., Posmentier, E. S., Sonder, L. J., and Fan, N.: Rethinking Craig and Gordon's approach to modeling isotopic compositions of marine boundary layer vapor, Atmos. Chem. Phys., 19, 4005–4024, doi:10.5194/acp-19-4005-2019, 2019.

Fiorella, R. P., Siler, N., Nusbaumer, J., and Noone, D. C.: Enhancing understanding of the hydrological cycle via pairing of process-oriented and isotope ratio tracers. J. Adv. Model. Earth Syst., 13, e2021MS002648. doi:10.1029/2021MS002648, 2021.

Galewsky, J., and Hurley, J. V.: An advection-condensation model for subtropical water vapor isotopic ratios, J. Geophys. Res.,115, D16116, doi:10.1029/2009JD013651, 2010.

Garstang, M., Tyson, P. D., Swap, R., Edwards, M., Kållberg, P., and Lindesay, J. A.: Horizontal and vertical transport of air over southern Africa, J. Geophys. Res., 101(D19), 23721– 23736, doi:10.1029/95JD0084410.1029/95JD00844, 1996.

Global Modeling and Assimilation Office, MERRA-2 tavgU_2d_flx_Nx: 2d, diurnal, Time-Averaged, Single-Level, Assimilation, Surface Flux Diagnostics V5.12.4, Greenbelt, MD, USA, Goddard Earth Sciences Data and Information Services Center (GES DISC) [data set], doi:~~10.5067/LUHPNWAKYIO3~~10.5067/LUHPNWAKYIO3, 2015.

Henze, D., Noone, D., and Toohey, D.: Aircraft measurements of water vapor heavy isotope ratios in the marine boundary layer and lower troposphere during ORACLES, Earth Syst. Sci. Data, 14, 1811–1829, doi:10.5194/essd-14-1811-2022, 2022.

Horita, J, and Wesolowski, D. J.: Liquid-vapor fractionation of oxygen and hydrogen isotopes of water from the freezing to the critical temperature, Geochimica et Cosmochimica Acta, 58, 3425-3437, doi:10.1016/0016-7037(94)90096-5, 1994.

IPCC, 2013: Climate Change 2013: The Physical Science Basis. Contribution of Working Group I to the Fifth Assessment Report of the Intergovernmental Panel on Climate Change [Stocker, T. F., Qin, D., Plattner, G.-K., Tignor, M., Allen, S. K., Boschung, J., Nauels, A., Xia, Y., Bex, V. and Midgley, P. M. (eds.)]. Cambridge University Press, Cambridge, United Kingdom and New York, NY, USA, in press, 2013.

Jones, C. R., Bretherton, C. S., and Blossey, P. N.: Fast stratocumulus time scale in mixed layer model and large eddy simulation, J. Adv. Model. Earth Syst., 6, 206–222, doi:10.1002/2013MS000289, 2014.

Jouzel, J., and Koster, R. D.: A reconsideration of the initial conditions used for stable water isotope models, J. Geophys. Res., 101(D17), 22933– 22938, doi:~~10.1029/96JD02362~~10.1029/96JD02362, 1996.

Kurita, N.: Water isotopic variability in response to mesoscale convective system over the tropical ocean, J. Geophys. Res. Atmos., 118, 10,376–10,390, doi:10.1002/jgrd.50754, 2013.

Latha, K. M., Badarinath, K. V. S., and Reddy, P. M.: Scavenging efficiency of rainfall on black carbon aerosols over an urban environment. Atmos. Sci. Lett., 6(3), 148–151. ~~doi:10.1002/asl.108~~doi:10.1002/asl.108, 2005.

Leon, D. C., Wang, Z., and Liu, D.: Climatology of drizzle in marine boundary layer clouds based on 1 year of data from CloudSat and Cloud-Aerosol Lidar and Infrared Pathfinder Satellite Observations (CALIPSO). J. Geophys. Res., 113 (D00A14), doi:10.1029/2008JD009 835, 2008.

Liu, X., Huey, L. G., Yokelson, R. J., Selimovic, V., Simpson, I. J., Müller, M., Jimenez, J. L., Campuzano-Jost, P., Beyersdorf, A. J., Blake, D. R., Butterfield, Z., Choi, Y., Crounse, J. D., Day, D. A., Diskin, G. S., Dubey, M. K., Fortner, E., Hanisco, T. F., Hu, W., King, L. E., Kleinman, L., Meinardi, S., Mikoviny, T., Onasch, T. B., Palm, B. B., Peischl, J., Pollack, I. B., Ryerson, T. B., Sachse, G. W., Sedlacek, A. J., Shilling, J. E., Springston, S., St. Clair, J. M., Tanner, D. J., Teng, A. P., Wennberg, P. O., Wisthaler, A., and Wolfe, G. M.: Airborne measurements of western U.S. wildfire emissions: Comparison with prescribed burning and air quality implications, J. Geophys. Res.-Atmos., 122, 6108–6129, doi:10.1002/2016jd026315, 2017.

Liu, D., Ding, S., Zhao, D., Hu, K., Yu, C., Hu, D., Wu, Y., Zhou, C., Tian, P., Liu, Q., Wu, Y., Zhang, J., Kong, S., Huang, M., Ding, D.: Black carbon emission and wet scavenging from surface to the top of boundary layer over Beijing region. J. Geophys. Res.-Atmos., 125, e2020JD033096. ~~doi:10.1029/2020JD033096. 2020.~~doi:10.1029/2020JD033096, 2020.

McNaughton, C. S., Clarke, A. D., Howell, S. G., Pinkerton, M., Anderson, B., Thornhill, L., Winstead, E., Hudgins, C., Dibb, J. E., Scheuer,E., and Maring, H.: Results from the DC-8 inlet characterization experiment (DICE): Airborne versus surface sampling of mineral dust and sea salt aerosols, Aerosol Sci. Tech., 41, 136–159, doi:10.1080/02786820601118406, 2007.

Merlivat, L., and Jouzel, J.: Global climatic interpretation of the deuterium-oxygen 18 relationship for precipitation, J. Geophys. Res., 84(C8), 5029– 5033, doi:~~10.1029/JC084iC08p05029~~10.1029/JC084iC08p05029, 1979.

Noone, D.: Pairing Measurements of the Water Vapor Isotope Ratio with Humidity to Deduce Atmospheric Moistening and Dehydration in the Tropical Midtroposphere, J. Climate, 25(13), 4476-4494, doi:10.1175/JCLI-D-11-00582.1, 2012.
Ohata, S., Moteki, N., Mori, T., Koike, M. and Kondodoi:10.1175/JCLI-D-11-00582.1, 2012.

Ohata, S., Moteki, N., Mori, T., Koike, M. and Kondo, Y.: A key process controlling the wet removal of aerosols: new observational evidence, Sci. Rep., 6, 34113. doi:10.1038/srep34113doi:10.1038/srep34113, 2016.

Paluch, I. R.: The entrainment mechanism in Colorado cumuli, J. Atmos. Sci., 36 , 2467–2478, doi:10.1175/1520-0469(1979)036<2467:TEMICC>2.0.CO;2doi:10.1175/1520-0469(1979)036<2467:TEMICC>2.0.CO;2, 1979.

Redemann, J., Wood, R., Zuidema, P., Doherty, S. J., Luna, B., LeBlanc, S. E., Diamond, M. S., Shinozuka, Y., Chang, I. Y., Ueyama, R., et al.,.: An overview of the ORACLES (ObseRvations of Aerosols above CLouds and their intEractionS) project: aerosol–cloud–radiation interactions in the southeast Atlantic basinAn overview of the ORACLES (ObseRvations of Aerosols above CLouds and their intEractionS) project: aerosol–cloud–radiation interactions in the southeast Atlantic basin, Atmos. Chem. Phys., 21 (3), 1507–1563, doi:10.5194/acp-21-1507-2021, 2021.

Risi, C., Noone, D., Worden, J., Frankenberg, C., Stiller, G., Kiefer, M., Funke, B., Walker, K., Bernath, P., Schneider, M., Wunch, D., Sherlock, V., Deutscher, N., Griffith, D., Wennberg, P. O., Strong, K., Smale, D., Mahieu, E., Barthlott, S., Hase, F., García, O., Notholt, J., Warneke, T., Toon, G., Sayres, D., Bony, S., Lee, J., Brown, D., Uemura, R., Sturm, C.: Process-evaluation of tropospheric humidity simulated by general circulation modelsusing water vapor isotopologues: 1. Comparison between models and observations, J. Geophys. Res.,117, D05303, doi:10.1029/2011JD016621, 2012.

Roberts, G. C. and Nenes, A.: A Continuous-Flow Streamwise Thermal-Gradient CCN Chamber for Atmospheric Measurements, Aerosol Sci. Technol., 39, 206–221, doi:10.1080/027868290913988, 2005.

Schubert, W. H., Wakefield, J. S., Steiner, E. J., and Cox, S. K.: Marine stratocumulus convection. Part II: Horizontally inhomogeneous solutions, J. Atmos. Sci., 36(7), 1308–1324, doi:10.1175/1520-0469(1979)036<1308:MSCPIH>2.0.CO;210.1175/1520-0469(1979)036<1308:MSCPIH>2.0.CO;2, 1979.

Schwarz, J. P., Gao, R. S., Fahey, D. W., Thomson, D. S., Watts, L. A., Wilson, J. C., Reeves, J. M., Darbeheshti, M., Baumgardner, D. G., Kok, G. L., Chung, S. H., Schulz, M., Hendricks, J., Lauer, A., Kärcher, B., Slowik, J. G., Rosenlof, K. H., Thompson, T. L., Langford, A. O., Loewenstein, M., and Aikin, K. C.: Single-particle measurements of midlatitude black carbon and light-scattering aerosols from the boundary layer to the lower stratosphere, J. Geophys. Res., 111, D16207, doi:10.1029/2006jd007076, 2006.

Steen-Larsen, H. C., Sveinbjörnsdottir, A. E., Jonsson, Th., Ritter, F., Bonne, J.-L., Masson-Delmotte, V., Sodemann, H., Blunier, T., Dahl-Jensen, D., and Vinther, B. M.: Moisture sources and synoptic to seasonal variability of North Atlantic water vapor isotopic composition, J. Geophys. Res. Atmos., 120, 5757–5774, doi:10.1002/2015JD023234, 2015.

Stephens, M., Turner, N., and Sandberg, J.: Particle identification by laser-induced incandescence in a solid-state laser cavity, Appl. Opt., 42, 3726–3736, doi:10.1364/ao.42.003726, 2003.

Textor, C., Schulz, M., Guibert, S., Kinne, S., Balkanski, Y., Bauer, S., Berntsen, T., Berglen, T., Boucher, O., Chin, M., Dentener, F., Diehl, T., Easter, R., Feichter, H., Fillmore, D., Ghan, S., Ginoux, P., Gong, S., Grini, A., Hendricks, J., Horowitz, L., Huang, P., Isaksen, I., Iversen, I., Kloster, S., Koch, D., Kirkevåg, A., Kristjansson, J. E., Krol, M., Lauer, A., Lamarque, J. F., Liu, X., Montanaro, V., Myhre, G., Penner, J., Pitari, G., Reddy, S., Seland, Ø., Stier, P., Takemura, T., and Tie, X.: Analysis and quantification of the diversities of aerosol life cycles within AeroCom, Atmos. Chem. Phys., 6, 1777–1813, doi:10.5194/acp-6-1777-2006, 2006.

Tritscher, T., Jurányi, Z., Martin, M., Chirico, R., Gysel, M., Heringa, M. F., DeCarlo, P. F., Sierau, B., Prévôt, A. S. H., Weingartner, E., and Baltensperger, U.: Changes of hygroscopicity and morphology during ageing of

diesel soot. Environ. Res. Lett., 6(3). ~~doi:10.1088/1748-9326/6/3/034026~~doi:10.1088/1748-9326/6/3/034026, 2011.

Twohy, C. H., Toohey, D. W., Levin, E. J. T., DeMott, P. J., Rainwater, B., Garofalo, L. A., Pothier, M. A., Farmer, D. K., Kreidenweis, S. M., Pokhrel, R. P., Murphy, S. M., Reeves, J. M., Moore, K. A., Fischer, E. V.: Biomass burning smoke and its influence on clouds over the western U. S., Geophys. Res. Lett., 48, e2021GL094224. ~~doi:10.1029/2021GL094224~~doi:10.1029/2021GL094224, 2021.

Van der Werf, G. R., Randerson, J. T., Giglio, L., Collatz, G. J., Mu, M., Kasibhatla, P. S., Morton, D. C., DeFries, R. S., Jin, Y., and van Leeuwen, T. T.: Global fire emissions and the contribution of deforestation, savanna, forest, agricultural, and peat fires (1997–2009), Atmos. Chem. Phys., 10, 11707-11735, doi:10.5194/acp-10-11707-2010, 2010.

Warner, M.: Introduction to PySPLIT: A Python Toolkit for NOAA ARL's HYSPLIT Model, Comput. Sci. Eng., vol. 20, no. 05, pp. 47-62, doi:10.1109/MCSE.2017.3301549, 2018.

Wood, R.: Cancellation of aerosol indirect effects in marine stratocumulus through cloud thinning, J. Atmos. Sci., 64, 2657–2669, doi:10.1175/JAS3942.1, 2007.

Wood, R.: Stratocumulus clouds. Review paper, Mon. Wea. Rev., 140, 2373-2423, 2012.

Zhang, R. Y., Khalizov, A. F., Pagels, J., Zhang, D., Xue, H. X., and McMurry, P. H.: Variability in morphology, hygroscopicity, and optical properties of soot aerosols during atmospheric processing. Proceedings of the National Academy of Sciences of the United States of America, 105(30), 10291–10296, ~~doi:10.1073/pnas.0804860105~~doi:10.1073/pnas.0804860105, 2008.

Zuberi, B., Johnson, K. S., Aleks, G. K., Molina, L. T., & Laskin, A.: Hydrophilic properties of aged soot. Geophys. Res. Lett., 32(1). ~~doi:10.1029/2004gl021496~~doi:10.1029/2004gl021496, 2005.

~~Zuidema, P., Redemann, J., Haywood, J., Wood, R., Piketh, S., Hipondoka, M., and Formenti~~Zuidema, P., Redemann, J., Haywood, J., Wood, R., Piketh, S., Hipondoka, M., and Formenti, P.: Interactions: Smoke and Clouds above the Southeast Atlantic Upcoming Field Campaigns Probe Absorbing Aerosol's Impact on Climate, Bull. Am. Meteorol. Soc., 19-23, doi:10.1175/BAMS-D-15-00082.1, 2016.